

1 **Sensitive and accurate dual wavelength**
2 **UV-VIS polarization detector for optical remote sensing**
3 **of tropospheric aerosols**

4
5 G. David, A. Miffre, B. Thomas and P. Rairoux

6
7 **Grégory David**¹, (g david@lasim.univ-lyon1.fr)

8 **Alain Miffre**^{1*}, (miffre@lasim.univ-lyon1.fr)

9 **Benjamin Thomas**¹, (bthomas@lasim.univ-lyon1.fr)

10 **Patrick Rairoux**¹, (rairoux@lasim.univ-lyon1.fr)

11
12 ¹ *Laboratoire de Spectrométrie Ionique et Moléculaire, CNRS, UMR 5579 Université Lyon 1,*

13 *10 rue da Byron, 69622 Villeurbanne, France*

14
15 * Corresponding author:

16 miffre@lasim.univ-lyon1.fr

17 fon: 0033-472.43.10.87

18 fax: 0033-472-43.15.07

19

20 **Abstract**

21 An UV-VIS polarization Lidar has been designed and specified for aerosols monitoring in the
22 troposphere, showing the ability to precisely address low particle depolarization ratios, in the range
23 of a few percents. Non-spherical particle backscattering coefficients as low as $5 \times 10^{-8} \text{ m}^{-1} \cdot \text{sr}^{-1}$ have
24 been measured and the particle depolarization ratio detection limit is 0.6 %. This achievement is
25 based on a well-designed detector with laser-specified optical components (polarizers, dichroic
26 beamsplitters) summarized in a synthetic detector transfer matrix. Hence, systematic biases are
27 drastically minimized. The detector matrix being diagonal, robust polarization calibration has been
28 achieved under real atmospheric conditions. This UV-VIS polarization detector measures particle
29 depolarization ratios over two orders of magnitude, from 0.6 up to 40 %, which is new, especially in
30 the UV where molecular scattering is strong. Hence, a calibrated UV polarization-resolved time-
31 altitude map is proposed for urban and free tropospheric aerosols up to 4 kilometres altitude, which is
32 also new. These sensitive and accurate UV-VIS polarization-resolved measurements enhance the
33 spatial and time evolution of non-spherical tropospheric particles, even in urban polluted areas. This
34 study shows the capability of polarization-resolved laser UV-VIS spectroscopy to specifically
35 address the light backscattering by spherical and non-spherical tropospheric aerosols.

36

37

38 **Keywords**

39 Polarization, UV-VIS Lidar, aerosols, Non-spherical particles.

40

41

42

43

44

45 **1. Introduction**

46

47 Atmospheric aerosols (or suspended particulate matter, PM) play a key role in the Earth atmosphere
48 radiative balance both directly, by light extinction, and indirectly, through complex processes
49 involving aerosols physical and chemical properties [1]. A well-known example is given in the
50 stratosphere by the ozone layer destruction in Polar Regions, related to anthropogenic polar
51 stratospheric clouds through complex photo-catalytic surface reactions [2-4]. In the troposphere,
52 atmospheric particles affect hydrometeor formation by acting as condensation nuclei [5]. Recent
53 studies have shown that PM may also modify the physical and chemical properties of the
54 atmospheric Planetary Boundary Layer (PBL), especially in urban polluted areas [6]. For climate
55 forcing assessments, the indirect role of particles on the radiative properties of atmospheric particles
56 must be quantitatively estimated. This task is very difficult since a complete physical and chemical
57 PM characterization is not yet achieved [7]. In particular, there is a need for measuring spatial and
58 temporal variations of PM-concentrations in urban polluted areas. One of the major limitations
59 originates from the lack of detailed knowledge on atmospheric aerosols optical properties, which
60 induces large uncertainties.

61

62 To face such a complexity, laser spectroscopy is of prime importance since PM light scattering and
63 extinction are nowadays the main applied optical properties to evaluate the PM-atmospheric content.
64 Several optical properties can be addressed by laser spectroscopy, as for example the scattering phase
65 function [8]. Laser spectroscopy can be applied to address the atmospheric particles chemical
66 composition, by studying their refractive index wavelength dependency [9]. Laser induced
67 fluorescence is another methodology to access to PM chemical composition also used to characterize
68 organic and biogenic atmospheric particles [10]. Along with these laser techniques, laser active
69 remote sensing (Lidar) is particularly interesting as it provides fast, reliable and range-resolved

70 access to the optical properties of an ensemble of atmospheric particles, under atmospheric
71 conditions of temperature and humidity [11, 12]. The laser excitation wavelength λ is often chosen in
72 the visible (VIS) or/and in the infra-red (IR) spectral range [10, 12, 13] while the ultraviolet (UV)
73 spectral range is rather seldom used [14-16]. In the meantime, atmospheric particles present a three-
74 modal size distribution with an ultra-fine mode (in the nanometer scale), a fine mode (in the range of
75 a few cents of nanometers) and a coarse mode (in the micrometer size range). While coarse particles
76 experience sedimentation processes and ultra-fine particles encounter aggregation and condensation
77 processes, fine particles have the longest lifetime in the atmosphere (several days). Hence, most
78 observed atmospheric particles are fine and in urban polluted areas, the number of fine particles can
79 exceed $1\ 000\ \text{part.cm}^{-3}$ [6]. To address high concentrated fine particles with laser remote sensing, it is
80 interesting to choose a laser excitation wavelength in the UV spectral range, where particles size
81 parameters ($x = 2\pi r/\lambda$ for an r equivalent sphere radius) often lead to scattering phase function
82 enhancements [17]. This is however challenging since in the UV spectral range, molecular scattering
83 may overcome particles scattering.

84

85 Among the major uncertainties involved in climate change modeling, the lack of knowledge on the
86 atmospheric particles shape is an essential point, especially in urban polluted areas, where
87 atmospheric aerosols may present a wide range of sizes and shapes. Applying the century-old
88 Lorenz-Mie formalism to tropospheric particles may lead to significant errors in climate change
89 modeling [18], as non-spherical particles scatter light differently from volume or surface-equivalent
90 spheres. In particular, orientation averaging over an ensemble of non-spherical particles does not lead
91 to the same scattering pattern as for spheres [19]. Hence, non-spherical particles are difficult to
92 address since no general analytical solution is available, except for some specific geometry far away
93 from the observed highly-irregularly shape of atmospheric particles [17]. However, in the Lidar
94 backward direction, the polarization of the phase function is unequivocally sensitive to particles

95 shape modifications [17], which makes the detection of this property attractive for laser remote
96 sensing. For spherical particles, the polarization state of the laser is preserved during the scattering
97 process. In contrast, scattering of light by an ensemble of randomly-oriented non-spherical particles
98 modify the polarization state of the laser. More precisely, as this polarization state is analyzed at a far
99 range compared to the particles size, randomly-oriented non-spherical particles exhibit a non-zero
100 polarization change [17], often called depolarization, whose magnitude (hereafter called the particles
101 depolarization ratio) is a signature of the particles shape. Hence, polarization-sensitive Lidar systems
102 can be used as particles shape indicators.

103

104 In this paper, we remotely address the polarization optical properties of tropospheric particles with a
105 new home-built dual-wavelength (UV-VIS) polarization Lidar. The addressed particles are present in
106 the PBL and in the free troposphere. The UV-light has been chosen to improve our sensitivity to the
107 fine particles mode while the dual-wavelength (UV-VIS) enables to address the spectral properties of
108 tropospheric urban aerosols. To our knowledge, tropospheric urban aerosols have only been studied
109 in the VIS or / and the IR spectral range [13,20]. Recent studies mainly focused on the remote
110 measurement of high particles depolarization ratios, in the range of 40 % as observed during volcanic
111 ash intrusion episodes [21-23] or in the 20 %-range, as for Saharan desert dust particles intrusion
112 events [24]. In between these rather seldom episodes, the particles load of an urban troposphere is
113 usually dominated by local sources of particulate matter, originating from petrochemical plants and
114 traffic-jam polluting the urban canopy [25]. There is no a priori evidence that such atmospheric PBL
115 particles be spherical. Rather low depolarization ratios, in the range of a few percents, may be
116 expected for urban tropospheric particles, but the magnitude of this depolarization needs to be
117 accurately evaluated to detect very small changes in the particles optical properties in general, and in
118 the particles shape in particular. Hence, in this paper, we concentrate on the measurement of low
119 particles depolarization ratios, in the range of few percents, which is the most frequently observed

120 situation in the Lyon troposphere. To trustworthy measure such low depolarization ratios, the
121 polarization detector must be very sensitive and very accurately designed. This is challenging since a
122 small system bias in the measured depolarization ratio, originating for example from an imperfection
123 on an optical component, may lead to substantial errors in the measured depolarization ratio.
124 Accordingly, the Lidar laser source and the polarization detector must be very accurately specified.
125 In this paper, a systematic study is proposed to specify the spectral and the polarization properties of
126 each optical component used in the dual-wavelength polarization detector. This specification has
127 been performed on a laboratory dedicated test bench. In the literature, manufacturer's specifications
128 are often trusted. Here, our approach is different since we combine UV and VIS-polarization
129 measurement in a single detector while optical specifications are rarely at the same level in these
130 spectral ranges and often given for continuous unpolarized white light, instead of the monochromatic
131 polarized pulses used in a polarization Lidar. Moreover, we are interested in (UV-VIS) low
132 depolarization ratios measurements so that any system bias must be carefully analyzed.

133

134 The novelty of this work is hence threefold. First, we consider the UV-VIS Lidar polarization
135 observation with depolarization ratios in the percent range, which is a very low value for atmospheric
136 Lidar observation. It induces strong constraints on the dual-wavelength polarization Lidar
137 experimental set-up and on its calibration. Secondly, the biases in the depolarization ratio
138 measurements are quantitatively estimated by considering the state-of-the-art for optical components
139 in the UV spectral range. Within our home-built polarization detector, a detection limit of 6×10^{-3} ,
140 comparable to the molecular depolarization, is achievable for remote polarization measurements.
141 Thirdly, examples of sensitive and accurate Lidar depolarization are presented in the PBL and the
142 free troposphere and analyzed in terms of PM laser light scattering in the UV and VIS-spectral range.
143 The paper is organized as follows. Section 2 is dedicated to theoretical considerations. Starting from
144 scattering of light by atmospheric particles, we analyze several possible system biases affecting the

145 depolarization ratio measurement at UV-VIS wavelengths. The sensitivity of these biases for
146 measuring low depolarization ratios is analyzed and for the first time, the role of the dichroic
147 beamsplitter, used for dual-wavelength polarization measurements, is addressed. To optimize our
148 sensitivity to low particle depolarization ratios, the sky background contribution to the Lidar signal is
149 then analyzed and polarization-resolved. In section 3, we first present our Lidar experimental set-up
150 (emitter, receiver and detector). Then, to fulfill the requirements derived in section 2, the spectral and
151 polarization properties of each detector optical component are specified in our laboratory. A detector
152 transfer matrix is provided to underline the performances of our dual-wavelength polarization
153 detector. As an output, we present in section 4 experimental measurements of tropospheric particles
154 depolarization in the percent range, in the UV and in the VIS-spectral range. To our knowledge for
155 the first time, a calibrated UV polarization-resolved time-altitude map is proposed for tropospheric
156 urban aerosols. The paper ends with a conclusion and outlooks.

157

158 **2. Dual-wavelength polarization Lidar methodology**

159

160 In this section, we focus on theoretical considerations for retrieving the particle backscattering
161 coefficient β_p and the particle depolarization ratio δ_p . In particular, we quantitatively analyze the
162 possible systematic biases affecting the δ_p -measurement at two wavelengths, by focusing on δ_p -
163 measurements in the range of a few percents.

164

165 **2.1 Scattering of light by atmospheric particles**

166

167 Light-scattering by an ensemble of particles, either spherical or not, can be described in the frame of
168 the scattering matrix \mathbf{F} , which relates the Stokes parameters of the incident and detected scattered
169 light beams [17]. In this formalism, an incident light wave (wave-vector \mathbf{k}_i , polarization $\boldsymbol{\pi}_i$) is

170 scattered by an ensemble of particles of arbitrary size and shape in all directions, the detector
171 direction defining the scattering angle θ and the scattering plane between the incident and scattered
172 light waves (wave-vector \mathbf{k} , polarization $\boldsymbol{\pi}$). The π_i and π -polarization states are usually defined with
173 respect to the light scattering plane, either parallel (p) or perpendicular (s) to this plane. In this paper,
174 our main concern is on the polarization state of the light wave backscattered ($\theta = 180^\circ$) by
175 tropospheric particles, probed with a linearly polarized laser beam propagating through the
176 atmosphere. In this Lidar backscattering case ($\theta = 180^\circ$), for randomly oriented particles, the \mathbf{F} -
177 matrix is diagonal and only depends on its first two elements F_{11} and F_{22} , which results in a linear
178 depolarization ratio δ :

179

$$180 \quad \delta = (F_{11} - F_{22}) / (F_{11} + F_{22}) \quad (1)$$

181

182 The depolarization ratio δ , determined by the F_{22}/F_{11} -ratio, is hence an intrinsic property of
183 randomly-oriented particulate matter, mainly governed by the particles shape [17]. It may also
184 depends on the laser wavelength λ and, as for F_{11} and F_{22} , on the size parameter x and on the complex
185 refractive index m [24]. Spherical particles, for which $F_{11} = F_{22}$, induce no depolarization ($\delta = 0$) in
186 contrary to non-spherical particles for which the equality $F_{11} = F_{22}$ no longer holds. Hence, the δ -ratio
187 can be used as a non-sphericity indicator of an ensemble of particles [17].

188

189 **a. Backscattering and depolarization in the atmosphere**

190 At altitude z above ground, the polarization components of the wave backscattered by the
191 atmosphere (intensity $\mathbf{I} = [I_p, I_s]^T$) are related to the polarization components of the incident laser
192 wave (intensity $\mathbf{I}_i = [I_{p,i}, I_{s,i}]^T$) through the well-known Lidar equation [26,27], assuming single-
193 scattering from the atmosphere :

194

195
$$\mathbf{I}(\lambda, z) = \frac{T^2(z)}{z^2} [\boldsymbol{\beta}](\lambda, z) \mathbf{I}_i + \mathbf{I}_{sb} \quad \text{with} \quad \beta(\lambda, z) = \begin{bmatrix} \beta_{//} & \beta_{\perp} \\ \beta_{\perp} & \beta_{//} \end{bmatrix} \quad (2)$$

196

197 for the specific case of Lidar elastic backscattering. The intensity is here considered instead of power
 198 or photons numbers to be independent of the surface detector. The Lidar equation is presented in the
 199 form of column-vectors to facilitate the discussion proposed in section 2.2. In the Lidar
 200 backscattering case, the incident laser linear polarization is often taken as a reference so that p or s-
 201 polarized components are preferably referred to as parallel (//) or perpendicular (\perp) with respect to
 202 the laser linear polarization. Hence, the $\boldsymbol{\beta}$ -matrix coefficients are defined with respect to the laser
 203 linear polarization. As shown in section 3, the relationship between the backscattered intensity vector
 204 \mathbf{I} and the detected intensity vector $\mathbf{I}^* = [I_{//}, I_{\perp}]^T$ can be expressed as follows:

205

206
$$\mathbf{I}^*(\lambda, z) = O(z) \times [\boldsymbol{\eta}(\lambda)] \mathbf{I}(\lambda, z) \quad (3)$$

207

208 where $O(z)$ is the overlap function to be specified in section 3.1 and $[\boldsymbol{\eta}(\lambda)]$ is the detector transfer
 209 matrix corresponding to the excitation laser wavelength λ , to be specified in section 3.3. Finally,
 210 $T(\lambda, z)$ denotes the optical transmission of the atmosphere and the intensity vector $\mathbf{I}_{sb} = [I_{sb,p}, I_{sb,s}]^T$
 211 represents the sky background contribution to the intensity Lidar signal \mathbf{I} , as described in section 2.3.

212

213 The Lidar signal \mathbf{I} results from atmospheric molecules N_2 and O_2 (subscript m) and particles
 214 (subscript p) backscattering. Application of the superposition principle to the volume backscattering
 215 coefficient β implies that $\beta = \beta_m + \beta_p$. As shown in [24], the particles backscattering coefficient β is
 216 linked to the scattering matrix \mathbf{F} by $\beta_{//} = (F_{11} + F_{22})/2$ and $\beta_{\perp} = (F_{11} - F_{22})/2$, so that, following
 217 equation (1), the atmosphere depolarization ratio δ is usually defined as: $\delta = \beta_{\perp}/\beta_{//}$. While the β -
 218 backscattering coefficient is additive (as for F_{11} and F_{22}), the δ -ratio is an intensive parameter.

219 However, in the atmosphere, both molecules and particles, which are a priori non-spherical,
220 contribute to the depolarization. Hence, a molecular (δ_m) and a particle (δ_p) depolarization ratio can
221 be defined. The molecular depolarization is due to molecules anisotropy, which provokes the
222 apparition of Raman ro-vibrational sidebands in the molecular backscattering spectrum, responsible
223 for light depolarization [28,29]. The relationship between δ , δ_p and δ_m has been first proposed in
224 [30]:

$$226 \quad \delta = \left(1 - \frac{1}{R_{//}}\right) \delta_p + \frac{\delta_m}{R_{//}} \quad (4)$$

227
228 where $R_{//} = 1 + \beta_{p, //} / \beta_{m, //}$ is known as the parallel Lidar R-ratio, representing the contrast of molecular
229 backscattering compared to particles backscattering (a particle-free or molecular atmosphere satisfies
230 to $R_{//} = 1$). As a result of the well-known λ^{-4} Rayleigh law, molecular backscattering in the UV-
231 spectral range (at $\lambda = 1064/3$ nm) is approximately five times more intense than in the VIS-spectral
232 range (at $\lambda = 1064/2$ nm). Hence, particles backscattering β_p and particles depolarization ratios δ_p
233 rather difficult to measure in the UV and a higher sensitivity and accuracy for the (β_p , δ_p)-
234 measurement are needed. Hence, in the literature, δ is sometimes preferably measured rather than δ_p
235 [15]. In a molecular atmosphere, vertical profiles of $\beta_{m, //}$ and $\beta_{m, \perp}$ have been determined from
236 molecular scattering computation, using reanalysis model from the European Centre for Medium-
237 Range Weather Forecasts (ECWMF). As shown by A. Behrendt [29], β_m and δ_m depend on the
238 detector daylight filter bandwidth ($\Delta\lambda$). Thanks to the spectral selectivity of our detector, δ_m has
239 negligible temperature dependence and deduced from molecular scattering theory. For $\Delta\lambda = 0.35$
240 nm, we get $\delta_m = 3.7 \times 10^{-3}$ at $\lambda = 355$ nm and 3.6×10^{-3} at $\lambda = 532$ nm.

241

242

243

244 **b. Particle backscattering and depolarization ratio (β_p , δ_p)-retrieval methodology**

245 In this paragraph, the methodology to derive β_p and δ_p is described. As shown in equation (4), $R_{//}$ and
246 δ have to be measured. The parallel Lidar R-ratio is computed by applying the Klett's inversion
247 algorithm [31] to correct for the particles extinction in the Lidar equation. A predefined value for the
248 particles backscatter-to-extinction ratio S_p is needed as well as a starting point z_0 for the inversion
249 algorithm, generally chosen at high altitudes. As detailed in [32], S_p depends on the particles
250 microphysics and is a priori varying with z-altitude. In the free troposphere, S_p -values of 50 sr have
251 been reported in the literature [33] and chosen in our inversion algorithm with an error bar of 5 sr. In
252 the Planetary Boundary Layer (PBL), moisture effects and chemical composition may strongly
253 influence the particles size distribution and consequently the S_p -value. We numerically calculated S_p
254 as a function of the relative humidity by using Mie and Rayleigh-Gans theory, for a realistic three-
255 mode particles size distribution detailed in [25], including soot, organics, sulphate and silicate
256 particles. In between the PBL and the free troposphere, we assumed a linear variation of S_p with z-
257 altitude starting at observed inversion layers. At altitude z, the accuracy on the Lidar ratio is derived
258 from the Klett's algorithm, by using the maximum and minimum values of S_p .

259

260 Vertical profiles of $\beta_{p, //}$ are retrieved from the parallel Lidar R-ratio computation by applying the
261 Klett's algorithm to the parallel Lidar intensity signal $I_{//}$. The $\beta_{p, \perp}$ -coefficient is very interesting to
262 derive as it is non-spherical particles specific, in contrary to $\beta_{p, //}$ and δ_p . By using equation (4) and the
263 δ_p -definition ($\delta_p = \beta_{p, \perp} / \beta_{p, //}$), we derive $\beta_{p, \perp} = (R_{//}\delta - \delta_m) \times \beta_{m, //}$, providing vertical profiles of $\beta_{p, \perp}$
264 as a function of z-altitude. The uncertainty on δ_p is derived from equation (4) and expresses as follows:

265

266
$$\frac{\Delta \delta_p}{\delta_p} = \frac{R_{//} \Delta \delta}{R_{//} \delta - \delta_m} + \frac{\delta \Delta R_{//}}{R_{//} \delta - \delta_m} + \frac{\Delta R_{//}}{R_{//} - 1} \quad (5)$$

267

268

269 2.2 Theoretical considerations for remote sensing of low depolarization ratios

270

271 The emission and the receiver Lidar systems, which are polarization-sensitive, may modify our
272 perception of the polarization backscattered by the atmosphere. To unambiguously determine
273 depolarization ratios, we have to correct for this system biases affecting the depolarization ratio
274 measurement at two wavelengths. Literature in this field is quite abundant. Pioneer work has been
275 done by J. Biele et al. [34] who developed an algorithm to remove the effect of a cross-talk
276 component small compared to the observed depolarization, in the case of polar stratospheric clouds
277 (PSC). Then, Adachi et al. [26] used a calibration method for accurate estimation of PSC
278 depolarization ratios estimates. In 2003, J. Reichardt et al. developed a method for determining δ by
279 using three elastic-backscatter Lidar signals [35]. In 2006, J.M. Alvarez developed a three-
280 measurement method to calibrate polarization-sensitive Lidars [36], further extended by V.F.
281 Freudenthaler et al. in 2009 to the case of desert dust particles [16]. Finally, the specific case of a
282 single-channel detector used to measure both polarization components has been studied in [37]. Each
283 of these algorithm correction schemes is well-suited for its designed case. Here, our main concern is
284 dedicated to low δ -measurements, in the range of a few percents. It is the subject of this paragraph to
285 quantitatively evaluate the system constraints to measure these low depolarization ratios. An
286 atmosphere having a low depolarization ratio δ , in the range of a few percents, is hence considered as
287 an input. In the absence of undesirable system bias, the measured depolarization δ^* would be equal
288 to δ but in general, δ^* differs from δ . Relations between δ^* and δ are here provided to account for
289 several sources of systematic errors presented in figure 1. The role of the dichroic beamsplitter,
290 introduced for dual-wavelength detection is analyzed in details. Each system bias is studied
291 separately to specifically address its contribution to δ^* , hence quantifying the relative error between
292 δ^* and δ , for δ -values in the percent range.

293 **Please insert figure 1 here.**

294 **a. Influence of a small unpolarized polarization component emitted in the atmosphere**

295 Here, we quantify the effect of a small unpolarized component in the emitted laser polarization on
296 the δ -measurement. This emitted unpolarized component may originate from the laser polarization
297 purity or / and from polarization-sensitive reflective mirrors from the emission optics. When the
298 polarization state of the emitted laser has two polarization components (i.e. $I_i = I_{i, //} + I_{i, \perp}$), a residual
299 polarization $\varepsilon = I_{i, \perp} / I_i \ll 1$ is emitted throughout the atmosphere (see figure 1a). In this case, even in
300 a non-depolarizing atmosphere ($\delta = 0$), the polarization state of the backscattered wave will have a
301 depolarized component, leading to a non-zero measured depolarization δ^* , i.e. $\delta^* \geq \varepsilon$. Equation (2)
302 shows that the parallel Lidar intensity $I_{//}$ is contaminated by the induced non-zero $\beta_{\perp} I_{i, \perp}$ term while
303 the perpendicular Lidar intensity I_{\perp} is contaminated by the term $\beta_{\perp} I_{i, //}$. Hence, after a few
304 calculations, δ^* can be expressed as a function of δ and ε , the bias parameter, as follows:

305

306
$$\delta^* = \frac{(1-\varepsilon) \delta + \varepsilon}{(1-\varepsilon) + \varepsilon \delta} \quad (6)$$

307

308 When $\delta = 10 \%$, a residual polarization $\varepsilon = 1 \%$ induces a measured depolarization $\delta^* = 11 \%$.
309 Moreover, as shown by equation (6) plotted in figure 1a, care should be taken when measuring low
310 depolarization ratios, in the 1 %-range: for $\delta = 1 \%$, the required ε -value to ensure that δ^* differs
311 from δ by no more than 1 %, is only equal to $10^{-2} \%$.

312

313 **b. Imperfect separation of polarization components, polarization cross-talks**

314 When separating the two polarization components $\pi = \{ //, \perp \}$, defined with respect to the laser linear
315 polarization, some leakage between the two polarization detection channels may occur, leading to an
316 imperfect polarization separation through cross-talk effects. To calculate the allowed leakage for
317 measuring δ -values in the range of a few percents, we introduce a cross-talk coefficient $CT_{//}$ to

318 characterize the leakage of the // -polarization channel into the \perp -polarization channel. As shown in
319 figure 1b, the parallel Lidar intensity $I_{//}$ is contaminated by the contribution from perpendicular
320 channel, having a CT_{\perp} -efficient, while removing the leakage contribution into the perpendicular
321 channel, which occurs with a $CT_{//}$ -efficiency. Hence, the measured parallel Lidar intensity $I^*_{//}$ is
322 given by: $I^*_{//} = (1 - CT_{//})I_{//} + CT_{\perp}I_{\perp}$. Symmetrically, the perpendicular Lidar intensity can be written
323 as $I^*_{\perp} = (1 - CT_{\perp})I_{\perp} + CT_{//}I_{//}$, as obtained from the $I^*_{//}$ -expression by simply exchanging the // and
324 \perp -subscripts, to satisfy photon energy conservation, hence introducing the CT_{\perp} cross-talk coefficient,
325 characterizing the leakage of the \perp -polarization channel into the // -polarization channel. δ^* is linked
326 to δ via the bias parameters $CT_{//}$ and CT_{\perp} as follows:

$$327$$

$$328 \quad \delta^* = \frac{(1 - CT_{\perp}) \delta + CT_{//}}{(1 - CT_{//}) + \delta CT_{\perp}} \quad (7)$$

329

330 For a $\delta = 10\%$ atmospheric input depolarization, a bias parameter of $CT_{//} = CT_{\perp} = 1\%$ leads to $\delta^* =$
331 11% . As shown by equation (7) and in figure 1b, care should be taken when measuring low
332 depolarization ratios, in the 1% -range: for $\delta = 1\%$, the same residual leakage induces a measured
333 depolarization δ^* of 2% , which represents a 100% -relative error.

334

335 **c. Misalignment between the transmitter and receiver polarization axes**

336 The polarization of backscattered photons is analyzed by projection on the polarization axes of the
337 Lidar detector. It is implicitly assumed that these polarization axes merge with the laser linear
338 polarization axes, so that the polarization plane of the transmitter and the receiver are in perfect
339 alignment. When a systematic offset-angle φ exists between the emitter and receiver axes (see figure
340 1c), as first described by J.M. Alvarez [36], the measured depolarization δ^* can be expressed as a
341 function of δ and the φ -angle as follows:

342

$$343 \quad \delta^* = G_\lambda \frac{\delta + \tan^2(\varphi)}{1 + \delta \tan^2(\varphi)} \quad (8)$$

344

345 where G_λ is the electro-optics calibration constant to be specified in section 3.4. The relative error
346 bar on δ is plotted in figure 1c for different φ angles. When $\delta = 10\%$, a residual offset angle of 5°
347 leads to $\delta^* = 10.7\%$ only. For $\delta = 1\%$, when $\varphi = 1^\circ$ (resp. 5°), $\delta^* = 1.03\%$ (resp. 1.76%). Varying
348 the offset angle φ can be used to calibrate our depolarization measurements to determine G_λ , as
349 proposed by J.M. Alvarez [36] and as detailed in section 3.4.

350

351 **d. Possible influence of a dichroic beamsplitter**

352 In dual-wavelength polarization Lidar detectors, a dichroic beamsplitter is often introduced to
353 differentiate the polarization state of backscattered photons at the two laser wavelengths. In this
354 paragraph, we analyze the possible bias introduced by such a dichroic beamsplitter on the
355 measurement of low depolarization ratios δ . To our knowledge, such a systematic study has never
356 been reported in the literature, where the dichroic beamsplitter is assumed to be polarization-
357 insensitive.

358

359 Let us consider a dichroic beamsplitter having R_p , R_s -reflectivity coefficients, defined with respect
360 to the dichroic beamsplitter incidence plane (a similar discussion could be held on the corresponding
361 transmission coefficients ($T_p = 1 - R_p$, $T_s = 1 - R_s$) coefficients). As a consequence of Fresnel's
362 formula, R_p generally differs from R_s ($R_p < R_s$), so that the reflection on the dichroic beamsplitter
363 does not modify the polarization state of the backscattered photons which remains linear but is
364 rotated. However, in the absence of polarization cross-talks, the dichroic beamsplitter induces no
365 leakage between the two polarization channels so that the difference in R_p , R_s -values is generally
366 simply taken into account during the polarization calibration procedure as a multiplicative constant.

367

368 The above situation implicitly assumes that the laser linear polarization axes merge with the p and s-
369 axes of the dichroic beamsplitter, so that the polarization plane of the transmitter and the dichroic
370 beamsplitter are in perfect alignment. When a systematic offset-angle θ_0 exists between the parallel
371 laser linear polarization axis and the p-axis of the dichroic beamsplitter (see figure 1d), polarization
372 cross-talks appear, which cannot be compensated during the polarization calibration procedure. We
373 quantified the effect of a non-zero offset angle θ_0 on the measurement of a low atmosphere
374 depolarization ratio δ . The corresponding calculations are detailed in appendix. In the presence of a
375 non-zero offset angle θ_0 , δ^* differs from δ :

376

$$377 \quad \delta^* = \frac{a^2 \cos^2 \theta_0 \sin^2 \theta_0 + \delta_0 (b - a \cos^2 \theta_0)^2}{(b - a \sin^2 \theta_0)^2 + \delta_0 a^2 \cos^2 \theta_0 \sin^2 \theta_0} \quad (9)$$

378

379 where the two coefficients $a = \sqrt{R_p} - \sqrt{R_s}$ and $b = \sqrt{R_p}$ are determined by the dichroic beamsplitter
380 R_p , R_s -reflectivity coefficients, as detailed in the appendix. When there is no offset angle, δ^* is
381 proportional to δ so that the corresponding proportionality coefficient R_s/R_p can be included in the
382 polarization calibration procedure. The relative error bar on δ is plotted in figure 1d for different
383 offset angles θ_0 , using $R_p = 72\%$ and $R_s = 94\%$.

384

385 **2.3 Sky background contribution to the polarized Lidar signal**

386

387 Scattering of sunlight by atmospheric molecules and particles is detected with the Lidar as a sky
388 background intensity, noted \mathbf{I}_{sb} in equation (2). Geophysical factors contribute to \mathbf{I}_{sb} such as the local
389 meteorological conditions or the relative positioning between the Sun and the Earth. Sun sky

390 scattering can drastically limit the range accessible to the perpendicular backscattering coefficient
391 $\beta_{p,\perp}$ and induce photon noise.

392

393 **a. Polarization components of sunlight scattered by the atmosphere**

394 To minimize sky background contribution, a field stop and a daylight suppression band-pass filter are
395 often inserted. In addition, we studied the polarization components of the sky background intensity
396 vector \mathbf{I}_{sb} . These p and s-sunlight polarization components are defined with respect to the solar
397 scattering plane, represented in figure 2a, together with the Lidar station (source and detector). The
398 scattering angle is the solar zenith angle θ_s , whose cosine is equal to $\cos(\theta_s) = \sin(\ell)\sin(\delta_s) +$
399 $\cos(\ell)\cos(\delta_s)\cos(h)$, where ℓ is Lidar station latitude, δ_s is the solar declination angle and h is the
400 local hour angle of the Sun. The p and s-polarization components of the sky intensity have been
401 calculated by assuming a standard molecular atmosphere. In the presence of aerosols, the p-polarized
402 component will increase (if these aerosols are spherical) or both polarized components will increase
403 (if some aerosols are non-spherical). By assuming an unpolarized sunlight, the ratio between p and s-
404 polarization components of \mathbf{I}_{sb} can be expressed by using the molecular differential scattering cross-
405 sections dependence on the scattering angle θ_s [28]:

406

$$407 \frac{I_{sb,p}}{I_{sb,s}} = \rho_0 + (1 - \rho_0)\cos^2(\theta_s) \quad (10)$$

408

409 where ρ_0 is the depolarization factor of the standard molecular atmosphere [38]. Hence, the p-
410 polarized component $I_{sb,p}$ is always below the s-component $I_{sb,s}$. We then projected these polarization
411 components on the $\{//,\perp\}$ -polarization Lidar axes by using figure 2a to obtain: $I_{sb,//} = \sin^2(h)I_{sb,p} +$
412 $\cos^2(h)I_{sb,s}$ and $I_{sb,\perp} = \cos^2(h)I_{sb,p} + \sin^2(h)I_{sb,s}$. Hence, from sunrise to sunset, the two polarization sky
413 background components cross twice during daytime.

414 **Please insert figure 2 here.**

415 **b. Experimental implications for measuring low depolarization ratios**

416 Figure 2b shows the measured sky background intensity I_{sb} as detected on each $\{\parallel, \perp\}$ -polarization
417 channel at $\lambda = 355$ nm on July 3rd 2011. These observations agree with the above $I_{sb,\parallel}$ and $I_{sb,\perp}$ -
418 expressions. In particular, when the sky background is at its maximum, $I_{sb,\perp}$ is below $I_{sb,\parallel}$. Hence, to
419 accurately measure depolarization ratios in the range of a few percents during daytime, it is
420 interesting to match the perpendicular polarization sky background component with the
421 perpendicular Lidar signal, which is approximately 100 times lower than the parallel Lidar signal.
422 This polarization matching can be accomplished by rotating the laser linear polarization with a half-
423 wave plate. In this situation, a new calibration is necessary (see section 3.4).

424

425 **3. UV-VIS polarization Lidar experimental set-up**

426

427 Lyon Lidar station (45.76 N, 4.83 E, France) is a home-built Lidar station, designed to remotely
428 measure the polarization-resolved backscattering properties of tropospheric aerosols with a high
429 spatial vertical resolution, a high sensitivity and a good accuracy. Hence, as shown in this section,
430 our Lidar experimental set-up has been designed by carefully analyzing the role of each optical
431 component on the spectral and polarization (λ , π) optical properties of the photons backscattered
432 from the troposphere. Polarization-resolved backscattering properties are studied at two wavelengths,
433 in the UV and the VIS spectral range (usually referred to as $2\beta + 2\delta$ -Lidar system in the Lidar
434 community). As explained in the introduction, the choice for UV-light enables an increased
435 sensitivity to fine particles [17]. In this section, we first describe our UV-VIS polarization-sensitive
436 Lidar experimental set-up (emitter, receiver and detector). Then, by using section 2.2 theoretical
437 considerations, we specify our detector by analyzing the specific role of each optical component
438 through laboratory and field measurements.

439

440 3.1 The Lidar emitter and the receiver

441

442 The Lidar emitter and receiver are represented in figure 3 and the corresponding optical components
443 are specified in Table 1. The laser head and the telescope are mounted on the same optical bench,
444 kept free from vibration from the floor by buffers. The laser head is a doubled (VIS) and tripled (UV)
445 Nd:YAG laser, emitting linearly polarized 10 ns duration laser pulses in the UV ($\lambda = 355$ nm) and the
446 VIS ($\lambda = 532$ nm) spectral range with a 10 Hz repetition rate, for energies of approximately 10 mJ in
447 the UV (20 mJ in the VIS spectral range). The laser head is fired for a sequence of 4000 laser shots
448 by externally triggering the laser flash lamps. Then, each laser beam enter the emitter optics system,
449 detailed in figure 3, composed of an emission polarizing beamsplitter cube (emission PBC), a half-
450 wavelength plate ($\lambda/2$) and a $\times 2.5$ beam expander (BE) to reduce the laser divergence down to 0.4
451 mrad while ensuring eye-safety. The emission PBC (Melles Griot, PBSO) improves the laser linear
452 polarization rate to better than 10 000:1. The half-wavelength plate is used to adjust the laser linear
453 polarization so that both wavelengths are emitted with the same linear vertical s-polarization. The 2λ -
454 laser beams are then combined with a 2''-diameter dichroic mirror (DM, Melles Griot LD5644)
455 which preserves the incident laser polarization ($T_s(355 \text{ nm}) > 99.5 \%$, $R_s(532 \text{ nm}) > 99.5 \%$) and
456 then directed towards the atmosphere in the Eastward direction by an elliptical mirror (M_E), also
457 used for redirecting backscattered photons on a 200 mm diameter $f/3$ -Newtonian telescope. During
458 the alignment procedure, the telescope has been precisely positioned with respect to the laser beam
459 axis, defined by two pinholes (see figure 3), by redirecting the 2λ -laser beams on the center of the
460 telescope primary mirror by using two pentaprisms, as developed for precise alignment procedures
461 (in the tens of micro-radian range) in quantum atom optics experiments [39]. We then identified the
462 position of the telescope's focus as the intersection point of the 2λ -laser beams, originating from
463 infinity to simulate backscattered photons from the atmosphere. The field of view (FOV) of the
464 telescope – 2.5 mrad – is determined by a 3 mm-diameter pinhole inserted at the telescope's focus,

465 and was chosen to minimize multiple scattering and solar sky background contributions to the Lidar
466 signals. Moreover, the pinhole diameter was determined with the constraint to achieve lowest
467 possible geometric compression, defined as the overlap function $O(z)$ between the laser beam
468 divergence and the receiver FOV. We numerically simulated the overlap function $O(z)$ as a function
469 of the laser initial diameter and beam divergence, the telescope's focal length, the primary and
470 secondary mirror diameters and the pinhole diameter (there is no off-axis distance). With our 3 mm-
471 diameter pinhole, the overlap function $O(z)$ is equal to unity for z-altitudes above 150 meters above
472 ground.

473

474 **Please insert figure 3 here.**

475

476 **3.2 Lyon home-built UV-VIS Lidar polarization detector**

477

478 The detector **D** is designed to efficiently separate backscattered photons with respect to their (λ, π) -
479 spectral and polarization optical properties. The **D**-inside optical composition is represented in figure
480 4 through a top view and a 3D-exploded side view of each polarization channel. The specifications of
481 the corresponding optical components are given in Table 2. **D** is housed in a small box, mounted on a
482 rigid test bench located in the (x,y) -plane. Two 1 mm-diameter pinholes, located at the entrance and
483 the detector exit, define the x-detector beam axis, which is materialized by a He-Ne laser, mounted
484 on the detector bench. Use of a diffuser and observation of diffraction rings allowed defining the
485 detector axis with a maximum deviation of 0.5 mm.m^{-1} , corresponding to 0.5 mrad. The He-Ne laser
486 was used to position the detector at right angle with respect to the telescope axis by using a third
487 pentaprism, hence merging the backscattered photons pathway with the detector beam axis (both
488 axes being materialized by lasers) with better than 1 milliradian accuracy. Moreover, the He-Ne laser

489 was used as an alignment laser, allowing **D** to be transportable, to allow mechanical alignment and
490 precise optical specification of the inside detector at the laboratory, as detailed in section 3.3.

491

492 **Please insert figure 4 here.**

493

494 In between the two 1 mm-pinholes, backscattered photons are wavelength separated by using two
495 dichroic beamsplitter (DB_λ), one for each λ -wavelength, which act as a low-pass filter selecting the
496 desired UV,VIS wavelength. Each DB_λ is positioned at 45° with respect to the detector x-axis and
497 each λ -channel is polarization-resolved by using two successive polarizing beamsplitter cubes (PBC,
498 see figure 4 exploded-view) which efficiently partitions the backscattered polarization π . Sky
499 background is reduced by a very selective band-pass interference filter (IF_λ) centered on the
500 molecular Cabannes's line. The resulting molecular depolarization δ_m is hence slightly dependent on
501 temperature variations: from 180 to 300 K, the error on δ_m is below 1 % [29]. Finally, (λ, π) -
502 backscattered photons are detected with a photomultiplier tube (PMT) having a 8 mm-diameter
503 photocathode. The resulting four channel (λ, π) photoelectrons are then sampled with two transient
504 recorder (Licel, 12 bits, 20 and 40 MHz sample rate) and a two channels acquisition board (National
505 Instruments MI, 12 bits, 50 MHz sample rate). A Labview program has been designed for externally
506 triggering the laser head and recording the (λ, π) range-resolved data acquisitions. Statistical error on
507 the Lidar signals is reduced by operating acquisitions over 4000 laser shots, then performing high
508 frequency filtering and range-averaging to lead to a final vertical resolution of 75 meters.

509

510 **3.3 Specifying the Lidar performances for the polarization measurement**

511

512 An ideal polarization Lidar has the ability to measure depolarization ratios with a high sensitivity
513 (from a few to several tens of percents) and a high accuracy (by minimizing statistical and systematic

514 errors). Statistical errors can be reduced by range and laser shots-averaging. In contrary, systematic
515 errors lead to system bias that are crucial for depolarization ratios measurements in the range of a
516 few percents, as described in section 2.2. In this paragraph, the performances of our home-built Lidar
517 (emitter, receiver and detector) for sensitive and accurate dual-wavelength polarization
518 measurements are specified through laboratory and field measurements. To fulfill the requirements
519 derived from theoretical considerations, the (λ, π) -spectral and polarization properties of each optical
520 component of the detector have been specified on a laboratory test bench. Manufacturer's
521 specifications cannot be used, since these specifications are generally achieved for unpolarized
522 continuous white light illumination, while the Lidar backscattered photons are polarized
523 monochromatic pulses. This laboratory specification gives the evolution of a backscattered photon
524 entering the detector **D** with (λ, π) -optical properties, throughout the detector box. A major
525 achievement of this work is the derivation of the detector transfer matrix $[\mathbf{M}_D(\lambda)]$, which relates the
526 intensity of backscattered photons between the detector entry and its exit, as a function of their $(\lambda,$
527 $\pi)$ -spectral and polarization optical properties. To our knowledge, such a specification is generally
528 not reported in the literature. Here, our approach is different since we are interested in low
529 atmospheric depolarization ratios, in the range of a few percents, which necessitates an accurate $(\lambda,$
530 $\pi)$ -detector specification.

531

532 **a. Specifying the Lidar emitter performances**

533 As a consequence of section 2.2.a, the polarization rate of the emitter unit must be carefully defined
534 for accurate measurements of low depolarization ratios in the 1 %-range. We hence performed a
535 laboratory experiment to control that the emitting optics (mirrors, dichroic beamsplitter) did not
536 change the linear polarization state of the laser beam ($I_p/I_s > 10\,000:1$ after the emission PBC). To
537 account for possible depolarization from the emission optics, which cannot be compensated by using
538 a half-wave plate, we inserted a plane mirror above the mirror (M_E) to reflect the incident laser beam

539 backwards down to the emission PBC. On the way back to the PBC, the \perp -component of the laser
540 beam, reflected by the emission PBC, can be analyzed with a supplementary PBC (not represented
541 on figure 3). We checked that $R_p I_{\parallel} \gg R_s I_{\perp}$ (with $R_p = 1 - T_p$ and $R_s = 1 - T_s$ defined with respect to
542 emission PBC). Hence, the cross-polarized component is negligible compared to the parallel
543 polarized-component, ensuring negligible polarization dependent reflectivity of the emission mirrors.

544

545 **b. Specifying the Lidar detector performances**

546

547 **Detector mechanical specification**

548 In our home-built detector, each mechanical component has been fixed with respect to the others on a
549 very rigid flat surface plate. During the detector building-up, to ensure precise mechanical alignment,
550 the detector box was transported directed at the emission optics system exit: the detector axis was
551 hence defined with respect to the laser beam axis, reported as a control with a thin quartz plate and a
552 He-Ne laser (see figure 5). The verticality of the DM_{λ} , crucial for accurate polarization
553 measurements (see section 2.2.d), has been adjusted with a one milliradian precision (by fixing each
554 DB_{λ} plate on a beam steering holder) and positioned at 45° with respect to the detector x-axis. Then,
555 the PBC's were precisely positioned to ensure that both detected polarization components probe the
556 same atmospheric volume. This crucial point has been checked through a laboratory experiment
557 where both polarization channels counted the same photon flux for an incident 45° linear
558 polarization. A similar experiment was conducted in the real atmosphere where the two polarization
559 Lidar signals were equally populated when orienting the $\lambda/2$ -emission plate at $\pm 45^\circ$ with respect to
560 the laser linear polarization. These mechanical specifications did not evolve for several months and
561 the use of the 2λ -polarization Lidar did not reveal any mechanical drift or severe deterioration of the
562 alignment.

563

564 **Specifying the DB_λ dichroic beamsplitters**

565 Ideally, the dichroic beamsplitters must reflect photons at the λ -wavelength while preserving their
566 polarization. In the literature, negligible attenuation of the optics before the PBC is often assumed
567 [16]. We have measured the R_p , R_s -reflectivity coefficients of each DB_λ plate (defined with respect to
568 the DB_λ incidence plane) on a dedicated laboratory test. As shown in figure 5 (top), our test bench is
569 composed of a two lenses optical system, having an $f/3$ numerical aperture to simulate collection of
570 backscattered light from the atmosphere by the $f/3$ Lidar's telescope. Table 2 presents the measured
571 (λ, π) reflectivity for each DM_λ -plate. Since R_p differs from R_s , the DM_λ vertical positioning
572 achieved during the mechanical alignment procedure is effectively crucial, as a consequence of
573 section 2.2.d theoretical development.

574

575 **Please insert figure 5 here.**

576

577 **Specifying the polarization PBC, polarization cross-talks**

578 As developed by J. Alvarez et al. [36], the insertion of a second polarizing beamsplitter cube (PBC)
579 ensures the polarization purity of the perpendicular polarization channel. In the UV (resp. VIS)
580 spectral range, manufacturers specifications (CVI Melles Griot) indicate $T_p > 90.0\%$ (resp. > 95.0
581 $\%$) and $R_s > 99.0\%$ (resp. 99.9%) for a 2° field of view ensured by our mechanical alignment. We
582 have measured the T_p , R_s -coefficients of each PBC on the dedicated laboratory test bench presented
583 in figure 5 (bottom), where the polarization state of the incident light is controlled by a $\lambda/2$ plate. The
584 VIS-PBC's exhibit T_p and R_s -values very close to 1 so that polarization cross-talk is fully negligible
585 at $\lambda = 532$ nm. Table 2 presents the measured T_p , R_s -coefficients for each UV-PBC. PBC_1 , which
586 exhibited the highest R_s -value, has been used as shared PBC, to improve the detected perpendicular
587 intensity, while PBC_2 (resp. PBC_3) was inserted on the parallel (resp. perpendicular) channel. Hence,
588 our measured polarization cross-talks coefficients are $CT_{//} = R_{p,1}T_{s,3} = 4 \times 10^{-6}$ and $CT_{\perp} = T_{s,1}T_{s,2} = 0$.

589 **Optimizing the detection of the backscattered photons flux**

590 The spectral separation of our UV-VIS detector is not perfect, due to the limited spectral rejection of
591 the dichroic beamsplitters, which are built for efficient operation in either the UV or the VIS spectral
592 range. However, in our detector, this contamination, measured with the laboratory test bench, is
593 completely negligible thanks to the use of very selective band-pass interference filters (OD 5 at $\lambda =$
594 532 nm for the IF_{UV} and at $\lambda = 355$ nm for the IF_{VIS}). Then, using our f/3 optical test bench, we
595 visualized the light pathway throughout the detector to prevent any eventual light blocking within the
596 telescope's FOV. Moreover, the parallel (perpendicular) polarized intensity $I_{//}$ (I_{\perp}) has been detected
597 in (at right angle to) the plane of the detector, while in the literature [16], the // -polarized signal is
598 often detected on the s-branch of the PBC since $R_s > T_p$. Since the difference between R_s and T_p is
599 very small, as explained in section 2.3, we matched the \perp -polarized Lidar signal, which is low and
600 hence difficult to accurately measure, with the lowest polarization component of the sky background
601 intensity (i.e. the \perp -polarized sky background intensity around midday). Finally, to improve the
602 Lidar signals quality, the position of the 8 mm-photocathode PMT has been optimized with respect
603 to lens (L_2). No photon counting was hence necessary, despite the very low Lidar I_{\perp} -intensity for low
604 depolarization ratios measurements.

605

606 **Detector transfer matrix**

607 The performances of our spectral and polarization-resolved detector can be summarized by writing
608 the detector transfer matrix $[\boldsymbol{\eta}(\lambda)]$ corresponding to the λ -detected wavelength, which relates the
609 backscattered photons intensity vector $\mathbf{I} = [I_p, I_s]^T$ to the detected backscattered photons intensity
610 vector $\mathbf{I}^* = [I_{//}^*, I_{\perp}^*]^T$ (see equation (3)). In this formalism, the role of the dichroic beamsplitter DB_{λ}
611 is summarized by a matrix \mathbf{M}_{DB} , detailed in the appendix, which is diagonal since the off-set angle θ_0
612 is null. Likewise, the π -separation achieved by the PBC's is taken into account with a diagonal

613 matrix (with better than 5×10^{-6} accuracy in the UV-spectral range). By noting that the p-component
 614 of the DB_λ corresponds to the s-polarized component of the PBC, we get:

615

$$616 \quad [\boldsymbol{\eta}_{(UV)}] = \begin{bmatrix} \mathbf{g}_{//,UV} & \\ \mathbf{g}_{\perp,UV} & \end{bmatrix} \begin{bmatrix} 0.99 & 0 \\ 4 \times 10^{-8} & 0.72 \end{bmatrix} \quad \text{and} \quad [\boldsymbol{\eta}_{(VIS)}] = \begin{bmatrix} \mathbf{g}_{//,VIS} & \\ \mathbf{g}_{\perp,VIS} & \end{bmatrix} \begin{bmatrix} 0.87 & 0 \\ 0 & 1 \end{bmatrix} \quad (11)$$

617

618 where $\mathbf{g}_{//,\lambda}$ and $\mathbf{g}_{\perp,\lambda}$ are the gains resulting from the applied PMT voltages on the λ -polarization
 619 channel. Then, for our dual-wavelength polarization detector, a detector transfer matrix \mathbf{M}_D can be
 620 written to relate the backscattered photons 2λ -intensity vector $\mathbf{I}_{2\lambda} = [I_{UV,p}, I_{UV,s}, I_{VIS,p}, I_{VIS,s}]^T$ to the
 621 detected backscattered photons 2λ -intensity vector $\mathbf{I}_{2\lambda}^* = [I_{UV,//}^*, I_{UV,\perp}^*, I_{VIS,//}^*, I_{VIS,\perp}^*]^T$:

622

$$623 \quad \mathbf{I}_{2\lambda}^* = [\mathbf{M}_D] \mathbf{I}_{2\lambda} \quad \text{with} \quad [\mathbf{M}_D] = \begin{bmatrix} [\boldsymbol{\eta}_{(UV)}] & 0 & 0 \\ 0 & 0 & 0 \\ 0 & 0 & [\boldsymbol{\eta}_{(VIS)}] \end{bmatrix} \quad (12)$$

624

625 to underline the spectral selectivity of our detector (no contamination between UV and VIS
 626 channels). As a conclusion, our $(\lambda, \boldsymbol{\pi})$ -optical detector is characterized by a bloc diagonal \mathbf{M}_D -matrix
 627 (with 4×10^{-8} accuracy) underlying that our detector efficiently partitions backscattered photons as a
 628 function of their polarization $\boldsymbol{\pi}$ (as a consequence of the use of two PBC) and their wavelength λ (as
 629 a consequence of OD 5-interference filters which ensure efficient wavelength separation without
 630 contamination).

631

632 **Multiple scattering effects**

633 Multiple scattering processes may induce some depolarization, even in the presence of spherical
 634 scatterers. Hence, to relate the atmosphere depolarization ratio to particles non-sphericity, we
 635 accounted for possible multiple scattering effects. The contribution of multiple scattering to the

636 measured depolarization ratio δ has been extensively studied in the literature [40,41]. In the case of
637 optically dense objects in the PBL, the depolarization ratio varies as an exponential law of the
638 telescope's FOV [42]. We have measured the atmosphere depolarization ratio δ as a function of the
639 receiver telescope's FOV. As shown by Tatarov et al. [42], for FOV below 8 mrad, the
640 depolarization ratio is almost independent on the receiving FOV, and hence exclusively due to
641 particles non-sphericity. Hence, our current 2.5 mrad receiving FOV, obtained by inserting a 3 mm-
642 diameter pinhole at the telescope's focus, is too small to provide depolarization via multiple
643 scattering processes.

644

645 **3.4 Calibration procedure for the polarization measurement**

646

647 Since the detector transfer matrix is diagonal, depolarization ratios are known with a multiplicative
648 constant that must be accurately determined for quantitative depolarization ratios measurements.
649 This multiplicative factor depends on the reflectivity and the transmission of the dichroic
650 beamsplitter and the PBC's, the IF_λ -transmission and the gain of the PMT at the applied voltages.
651 Since the relation between the PMT-gain and the applied voltage is not precisely known, a
652 calibration procedure is necessary to determine the calibration constant corresponding to the λ -
653 channel, hereafter referred to as the electro-optics calibration constant G_λ . As shown by J. Alvarez
654 [36], in the absence of misalignment between the laser linear polarization and the parallel axis of the
655 detector PBC, the measured depolarization ratio δ^* is related to the atmosphere depolarization δ by
656 the simple relation $\delta^* = G_\lambda \delta$, as detailed in equation (8). This section presents our experimental
657 determination of G_λ for the two 355 and 532 nm polarization channels by using Alvarez's method
658 [36]. To retrieve G_λ , we introduced a controlled offset angle φ between the laser linear polarization
659 and the parallel axis of the detector's PBC [36]. In this case, the behavior of δ as a function of δ_0
660 depends on the φ -angle with a law that is given in equation (8). These controlled amounts of

661 polarization cross-talks can be used to retrieve G_λ by adjusting δ as a function of the φ calibration
662 angle under stable atmospheric conditions. Other methods [16,29] are applicable but molecular
663 calibration is of limited accuracy since a particle-free atmosphere does not rigorously exist. Setting φ
664 to $\pm 45^\circ$ leads to the same backscattered intensity on each polarization channel, so that G_λ is then
665 simply equal to δ^*/δ [16]. The accuracy of this $\pm 45^\circ$ calibration method is adequate but limited by
666 the possibility to have an exact 90° rotation control and by possible PMT-saturation (for $\delta = 1\%$, I_\perp
667 is multiply by 50). Figure 6 presents the results of our calibration procedure, obtained by applying
668 Alvarez's method. Two calibration curves are provided for backscattering at 355 nm and at 532 nm.
669 The G_λ -value is retrieved by adjusting the measured points with their error bar by using equation (8).
670 We hence obtained $G_{UV} = 29.16 \pm 0.22$ and $G_{VIS} = 16.69 \pm 0.23$, the accuracy originating from the
671 use of several φ -calibration angles. With this method, the maximum φ -angle value used is 23° , which
672 limits possible PMT-saturation effects (this time, for $\delta = 1\%$, I_\perp is multiplied by 17 which respects
673 the PMT linearity). Hence, G_λ is known with better than 2 %-accuracy.

674 **Please insert figure 6 here.**

675

676 **4. Application to free troposphere and urban aerosols remote sensing**

677

678 In this section, our dual wavelength polarization detector is used to remotely measure the
679 polarization backscattering properties of tropospheric aerosols at Lyon. Hence, the sensitivity and the
680 accuracy of our detector for (β_p, δ_p) -measurements are evaluated under atmospheric conditions, as a
681 consequence of the theoretical considerations derived in section 2 and the specification of our
682 detector achieved in section 3.

683

684 High particles depolarization ratios have been measured in the Lyon troposphere during volcanic and
685 dust episodes that occurred at Lyon during the last two years, as a consequence of the highly-

686 irregularly shape of volcanic ash and Saharan dust particles. These events have been an opportunity
687 to test the ability of our detector to measure high UV-particle depolarization ratios, as high as $(40.5$
688 $\pm 8.0)$ % for volcanic ash particles at 4 kilometers altitude [22], or $\delta_p = (19.5 \pm 3.5)$ % for Saharan
689 dust particles [24]. The achieved UV-sensitivity, specified in section 3, allowed distinguishing
690 different volcanic layers, having different depolarization ratios, with 75 meters-vertical resolution
691 [21]. However, no measurements were made in the VIS spectral range.

692

693 As explained in the introduction, we here focus on the measurement of low depolarization ratios, in
694 the range of few percents, which is the most frequently observed situation in the Lyon troposphere.
695 In figure 7, we present a time-altitude map, showing the spatial and temporal evolution of the optical
696 properties of Lyon tropospheric particles, on 18th October 2011 between 13h30 and 18h00 up to 4
697 kilometers altitude. The plotted optical properties are the parallel and perpendicular particle
698 backscattering coefficient $\beta_{p,\parallel}$ and $\beta_{p,\perp}$ and the corresponding particle depolarization ratio δ_p , in both
699 the UV and the VIS spectral range. To facilitate the interpretation of these data, the color scales have
700 been adjusted in each color plot, to put light on the achieved sensitivity. To our knowledge, the
701 calibrated UV-particle depolarization δ_p -map, achieved for tropospheric urban particles, is a new
702 achievement. These plots show that the observed tropospheric particles are mainly distributed into
703 two major distinct atmospheric layers: the PBL (for altitudes below 1 km), outlined by a strong
704 temperature inversion observed at 1 km altitude, and the free troposphere (for altitudes above 1 km).
705 In the PBL, the layer is relatively homogeneous, while in the free troposphere, two secondary layers
706 (around 2 and 3 km altitude), with temporal non homogeneity, can be distinguished.

707

708 In the PBL, the $\beta_{p,\parallel}$ -values are high in the UV, in the range of $5 \times 10^{-6} \text{ m}^{-1}.\text{sr}^{-1}$, a value usually
709 observed during a smog episode [25]. Within our error bars (to be seen in figure 8), the $\beta_{p,\parallel}$ -values
710 are significantly lower than in the VIS. This behavior can be explained by considering that

711 backscattering in the UV more efficiently addresses ultra-fine and fine particles than backscattering
712 in the VIS spectral range [17]. Therefore, in the PBL, particles are mostly distributed in the fine
713 particle mode of the particles size distribution, with radii typically around 300 nm [43]. In the free
714 troposphere, the VIS $\beta_{p,\parallel}$ -values are often comparable to the UV $\beta_{p,\parallel}$ -values, so that both fine and
715 coarse particles modes are addressed.

716

717 While the $\beta_{p,\parallel}$ -Lidar channel is sensitive to both spherical and non-spherical particles, the $\beta_{p,\perp}$ -Lidar
718 channel is non-spherical particles specific [24]. Hence, the $\beta_{p,\perp}$ -map provides the spatial and
719 temporal distribution of tropospheric non-spherical particles. The sensitivity achieved in section 3
720 enables to measure very small $\beta_{p,\perp}$ -values, as low as $3 \times 10^{-8} \text{ m}^{-1} \cdot \text{sr}^{-1}$. Therefore, in the PBL, for
721 altitudes below 500 meters, even non-spherical coarse particles can be detected in the VIS. Due to
722 their inertia, these particles seem unable to reach higher altitudes by convection. In the meanwhile, in
723 the UV, the $\beta_{p,\perp}$ -map exhibits non-spherical fine particles (more efficiently detected on the UV-
724 polarization channels), following the convective atmospheric movements up to the PBL, after a wind
725 speed change occurred at 15 h. Hence, despite the very low measured depolarization ratios, the
726 dynamics of non-spherical particles is retraced. Only a few percent particle depolarization ratio are
727 measured in the UV, since $\beta_{p,\parallel}$ is very high due to the smog episode. In the VIS, δ_p is higher as a
728 consequence of low concentration coarse mode particles. In the free troposphere, in the VIS, non-
729 spherical particles lay into two relatively homogeneous major layers having different thicknesses.
730 The different distribution observed in the UV indicates that the non-spherical particles size
731 distribution is non homogeneous in the free troposphere. The corresponding δ_p -measurements exhibit
732 particle depolarization ratios between 6 and 10 %. The meteorological analysis enables to think that
733 the corresponding air masses originate from the Atlantic region and contain non-spherical particles,
734 such as sea-salt particles, as confirmed by laboratory measurements which reveal an intrinsic
735 depolarization ratio in the 10 %-range [44].

736 **Please insert figure 7 here.**

737

738 Vertical profiles of $\beta_{p,\parallel}$, $\beta_{p,\perp}$ and δ_p are proposed in figure 8 in the UV and the VIS at 14h45 to
739 provide the error bar on each measured coefficient, hence addressing our achieved sensitivity and
740 accuracy. As observed during tropospheric volcanic ash events [21] or in the stratosphere [30],
741 scattering does not necessarily correlate with depolarization, since δ does not follow the
742 superposition principle as described in section 2.1. Vertical profiles are limited up to 4 km to
743 preserve a high signal-to-noise range ratio. The proposed error bars result from precise R_{\parallel} -evaluation
744 and accurate δ -measurement. Within our error bars, at 14h45, particles in the PBL are more
745 efficiently detected in the UV-channel, indicating that these particles are preferably fine low
746 depolarizing particles. In the free troposphere, the depolarization behavior results from a complex
747 mixing of fine and coarse particles. Despite strong UV-molecular scattering, our error bars are very
748 low as a consequence of our very precise calibration procedure and our laboratory detector building
749 up, optimization and specification. The relative error on the β_p -coefficient does not exceed 10 %
750 while the maximum error on the particle depolarization ratio δ_p is 23 %, calculated by using equation
751 (5). To our knowledge, such values have never been reported in the literature, especially in the UV
752 spectral range. Moreover, very low depolarization ratios, as low as only a few percents, are measured
753 with accuracy. In the UV (resp. VIS), at $z = 800$ m, we measured δ_p (UV) = (4.2 ± 0.3) % (resp. δ_p
754 (VIS) = (3.4 ± 0.3) % at 14h45. Hence, our detection limit is 2×0.3 % = 0.6 %, a value comparable
755 to the molecular depolarization. As a conclusion, the particle depolarization in the PBL should be
756 considered as different from zero.

757 **Please insert figure 8 here.**

758

759

760

761 **5. Conclusions**

762

763 In this paper, a dual-wavelength polarization Lidar detector has been built, optimized, specified and
764 operated, by starting from the very beginning. Our new detector provides remote measurements of
765 the polarization-resolved backscattering properties of tropospheric aerosols, in the UV (at 355 nm)
766 and the VIS (at 532 nm) spectral range, with a high spatial vertical resolution, a high sensitivity and a
767 reliable accuracy. To our knowledge for the first time, a calibrated particle depolarization δ_p -map has
768 been achieved in the UV spectral range for tropospheric particles, despite strong molecular
769 scattering.

770

771 We first identified the relevant parameters for measuring low particle depolarization ratios, in the
772 range of a few percents, from a theoretical point of view (see section 2). To trustworthily evaluate
773 such depolarization ratios, it is necessary to evaluate the different system biases altering the
774 backscattered polarization. In particular, the sensitivity of each bias for low depolarization
775 measurements has been quantified in section 2. Then, in section 3, the spectral and polarization
776 properties of our dual-wavelength polarization detector have been specified on a laboratory dedicated
777 test bench, to satisfy the section 2 identified requirements. The role of the dichroic beamsplitter used
778 for dual-wavelengths measurements, has been precisely addressed. Moreover, the backscattered
779 photons flux has been optimized and the detector specifications have been reported in a synthetic
780 block-diagonal detector transfer matrix, underlying the partitioning efficiency of backscattered
781 photons as a function of their polarization π (as a consequence of the use of two PBC) and their
782 wavelength λ (as a consequence of very selective IF ensuring efficient wavelength separation without
783 contamination). After accurate polarization calibration procedure, we tested the sensitivity and
784 accuracy of our (λ, π) -Lidar detector under real atmospheric conditions by measuring particles
785 backscattering coefficient (β_p) and depolarization ratio (δ_p) for tropospheric aerosols. The β_p -

786 coefficient, derived from the Klett's algorithm, has been calculated from an extinction-to-backscatter
787 ratio S_p , numerically evaluated as a function of the PBL-thermodynamics by using a three-mode
788 aerosols size distribution detailed in [25]. Accurate Raman Lidar measurements or HSRL can be an
789 alternative methodology to derive β_p [45]. The polarization detector measures UV-particle
790 depolarization ratios over almost two orders of magnitude, from 0.6 % (detection limit very close to
791 the molecular depolarization), up to 40 %, as observed during volcanic ash episodes. Such
792 depolarization ratios are remotely measured over 4 kilometers, with a vertical range resolution of
793 only 75 meters. The achieved sensitivity and accuracy enable to precisely retrace the polarization and
794 backscattering properties of tropospheric aerosols, even in the presence of low depolarizing particles.
795 Hence, conclusions on atmospheric physics can be drawn. The observed β_p and δ_p - time-altitude
796 maps exhibit a different behavior in the UV and the VIS spectral range, as a consequence of the
797 higher scattering efficiency of fine particles in the UV [17]. Hence, fine and coarse particles are
798 addressed in the PBL (where a smog episode is observed) and in the free troposphere (where sea-salt
799 particles are to be seen) with our dual-wavelength polarization Lidar. Spectroscopy of nano-sized
800 atmospheric particles can then be remotely achieved.

801

802 As a conclusion, achieving sensitive and accurate low depolarization ratios measurement is difficult,
803 especially in the UV spectral range where molecular scattering is strong. This difficulty obliged us to
804 precisely analyze the relevant parameters for trustworthy measure particle depolarization ratios.
805 Consequently, a major achievement of this work is the observation of non-spherical tropospheric
806 particles in the PBL, in the UV and the VIS spectral range. This dual-wavelength particle
807 depolarization ratio measurement may open new insights for further use in retrieval schemes aimed
808 at deriving the particles microphysics. Knowledge on the solid-state content of the atmosphere may
809 enable to explore new pathways in atmospheric photo-chemistry, especially for photo-catalytically
810 heterogeneous reactions occurring at the PM surface [46]. In this context, knowledge of the particle

811 linear depolarization ratio δ_p at two wavelengths, namely the UV and the VIS, is essential, as detailed
812 in several theoretical publications [47,48], provided that sensitive and accurate Lidar polarization
813 measurements are achieved.

814

815 **6. Acknowledgments**

816 The authors thank Marc Néri for his help in fine mechanics and Région Rhône-Alpes for research
817 grant.

818

819 **7. Appendix**

820 In this appendix, we investigate the effect of a misalignment of the dichroic beamsplitter on the
821 measured depolarization ratio δ^* . To parameterize the magnitude and the direction of this
822 misalignment, we introduce an offset angle θ_0 defined in figure 1.d as the angle between the parallel
823 laser linear polarization and the p-axis of the dichroic beamsplitter (defined with respect to the
824 dichroic beamsplitter plane of incidence). The aim of this appendix is to derive the relationship
825 between the measured depolarization δ^* and the atmosphere depolarization δ as a function of the θ_0
826 offset angle and the R_p , R_s -reflectivity coefficients of the dichroic beamsplitter, hence justifying
827 equation (9).

828

829 The incident electric field \mathbf{E}_i on the dichroic beamsplitter can be written in the two involved
830 mathematical bases, namely the ($//$, \perp)-Lidar polarization basis and the (p,s)-dichroic beamsplitter
831 basis. As shown by figure 1.d, a θ_0 -rotation angle enables to change from one basis to the other. We
832 projected the incident electric field vector \mathbf{E}_i of backscattered photons on the (p, s)-polarization basis
833 to express the electric field vector \mathbf{E}_r of the reflected wave:

834

$$835 \begin{bmatrix} \mathbf{E}_{r, //} \\ \mathbf{E}_{r, \perp} \end{bmatrix} = \begin{bmatrix} r_p \cos(\theta_0) & -r_s \sin(\theta_0) \\ r_p \sin(\theta_0) & r_s \cos(\theta_0) \end{bmatrix} \begin{bmatrix} \mathbf{E}_{i,p} \\ \mathbf{E}_{i,s} \end{bmatrix} \quad (\text{A-1})$$

836 In this expression, we have introduced amplitude field reflectivity coefficients r_p and r_s defined as r_p
837 $= E_{r,p}/E_{i,p}$ and $r_s = E_{r,s} / E_{i,s}$ where $E_{i,p}$ and $E_{i,s}$ are the components of \mathbf{E}_i in the (p,s)-dichroic
838 beamsplitter basis (the same notations are used for the reflected field \mathbf{E}_r). Then, by projecting the
839 incident electric field in the ($//, \perp$)-polarization basis, equation (A.1) becomes:

840

$$841 \quad \mathbf{E}_r = [\mathbf{m}_{DB}] \mathbf{E}_i \quad \text{with} \quad \mathbf{m}_{DB} = \begin{bmatrix} b - a \sin^2 \theta_0 & a \cos \theta_0 \sin \theta_0 \\ a \cos \theta_0 \sin \theta_0 & b - a \cos^2 \theta_0 \end{bmatrix} \quad (\text{A-2})$$

842

843 where the \mathbf{m}_{DB} -matrix relates the incident and reflected electric fields in the ($//, \perp$)-polarization basis
844 and the two coefficients $a = r_p - r_s = \sqrt{R_p} - \sqrt{R_s}$ and $b = r_p = \sqrt{R_p}$ are determined by the dichroic
845 beamsplitter R_p, R_s -reflectivity coefficients. Hence, reflection (or symmetrically transmission) on
846 the dichroic beamsplitter induces a rotation of the linear polarization state of the light. In the ideal
847 case, the dichroic beamsplitter is vertical, so that the p-axis is horizontal and θ_0 is zero. If we
848 exchange the $//$ and \perp -polarization channels, θ_0 is then $\pi/2$. In both cases ($\theta_0 = 0$ or $\pi/2$), the \mathbf{m}_{DB} -
849 matrix is diagonal so that no cross-talk is induced. To derive the measured depolarization ratio δ^* as
850 a function of δ , we now introduce intensities, proportional to the square of the electric field. Hence,
851 equation (A.2) can be written for laser intensities vectors \mathbf{I}_r and \mathbf{I}_i . By removing proportionality
852 constants (which disappear in the δ^* -calculation), we get:

853

$$854 \quad \mathbf{I}_r = [\mathbf{M}_{DB}] \mathbf{I}_i \quad \text{with} \quad \mathbf{M}_{DB} = \begin{bmatrix} (b - a \sin^2 \theta_0)^2 & a^2 \cos^2 \theta_0 \sin^2 \theta_0 \\ a^2 \cos^2 \theta_0 \sin^2 \theta_0 & (b - a \cos^2 \theta_0)^2 \end{bmatrix} \quad (\text{A-3})$$

855

856 by noting that the ($//, \perp$)-polarization basis is orthogonal. As expected, the \mathbf{M}_{DB} -matrix is diagonal in
857 the absence of offset angle θ_0 (i.e. if $\theta_0 = 0$ or $\pi/2$). By noting that $\delta^* = I_{r,\perp}/I_{r,//}$ while $\delta = I_{i,\perp}/I_{i,//}$, we
858 get the following relationship between δ, δ_0 and θ_0 , which is identical to equation (9):

859

860
$$\delta^* = \frac{a^2 \cos^2 \theta_0 \sin^2 \theta_0 + \delta_0 (b - a \cos^2 \theta_0)^2}{(b - a \sin^2 \theta_0)^2 + \delta_0 a^2 \cos^2 \theta_0 \sin^2 \theta_0} \quad (\text{A.4})$$

861

862 where the two coefficients $a = r_p - r_s = \sqrt{R_p} - \sqrt{R_s}$ and $b = r_p = \sqrt{R_p}$ are determined by the dichroic
863 beamsplitter R_p , R_s -reflectivity coefficients.

864

865 **8. References**

866

867 [1] S. Twomey, "The Influence of Pollution on the Shortwave Albedo of Clouds", *J. Atmos. Sci.*, **34**,
868 1149–52, (1977).

869

870 [2] L.A. Barrie, J.W. Bottenheim, R.C.Schnell, P.J. Crutzen, P.J. and R.A.Rasmussen, "Ozone
871 destruction and photochemical reactions at polar sunrise in the lower Arctic atmosphere", *Nature*,
872 **334**, 138–141, (1998)

873

874 [3] V. Rizi et al., "Trajectory studies of polar stratospheric cloud lidar observations at Sodankyla
875 (Finland) during SESAME: Comparison with box model results of particle evolution", *J. Atm.*
876 *Chem.*, **32**, 165-181, (1999).

877

878 [4] G.L. Manney et al., Unprecedented Arctic ozone loss in 2011, *Nature*, **478**, 469-U65, (2011).

879

880 [5] SS. Gunthe et al., "Cloud condensation nuclei (CCN) from fresh and aged air pollution in the
881 megacity region of Beijing", *Atm. Chem. Phys.*, **11**, 11023-11039, (2011).

882

883 [6] O. Favez et al., ‘Inter-comparison of source apportionment models for the estimation of wood
884 burning aerosols during wintertime in an Alpine city (Grenoble, France)’, *Atm. Chem. Phys.*, **10**,
885 5295-5314, (2010).

886

887 [7] IPCC, 2007, S. Solomon, D. Qin, M. Manning, Z. Chen, M. Marquis, K.B. Averyt, M. Tignor
888 and H.L. Miller, "Climate Change 2007: The Physical Science Basis. Contribution of Working
889 Group I to the Fourth Assessment Report of the Intergovernmental Panel on Climate Change",
890 Cambridge University Press ed. , Cambridge United Kingdom and New York USA, (2007).

891

892 [8] J. F. Gayet, O. Crépel, J. F. Fournol, S. Oshchepkov, "A new airborne polar Nephelometer for
893 the measurements of optical and microphysical cloud properties, Part I: Theoretical design", *Ann.*
894 *Geophysicae*, **15**, 451-459 (1997).

895

896 [9] M. Lang-Yona, Y. Rudich, E. Segre, E. Dinar, A. Abo-Riziq, “Complex Refractive Indices of
897 Aerosols Retrieved by Continuous Wave-Cavity Ring Down Aerosol Spectrometer”, *An. Chem.*,
898 **81**, 1762-1769, (2009).

899

900 [10] G. Mejean, J. Kasparian, J. Yu, S. Frey, E. Salmon, JP Wolf, “Remote detection and
901 identification of biological aerosols using a femtosecond terawatt lidar system”, *App. Phys. B*, **78** ,
902 535-537 , (2004).

903

904 [11] I. Veselovskii, et al., “Application of randomly oriented spheroids for retrieval of dust particle
905 parameters from multiwavelength lidar measurements”, *J. Geophys. Res*, **115**, D21203, (2010).

- 906 [12] M. Kacenelenbogen et al., “An accuracy assessment of the CALIOP/CALIPSO version
907 2/version 3 daytime aerosol extinction product based on a detailed multi-sensor, multi-platform case
908 study”, *Atm. Chem. Phys.*, **11**, 3981-4000, (2011).
- 909
- 910 [13] N. Sugimoto et al., “ Observation of dust and anthropogenic aerosol plumes in the Northwest
911 Pacific with a two-wavelength polarization lidar on board the research vessel Mirai”, *Geophys. Res.
912 Lett.* **29**, doi:10.1029/2002GL015112, (2002).
- 913
- 914 [14] J. Reichardt et al., “Optical properties of PSC Ia-enhanced at UV and visible wavelengths:
915 Model and observations”, *Geophys. Res. Lett.*, **27**, 201-204, (2000).
- 916
- 917 [15] R.Adam de Villiers, G. Ancellet, J. Pelon, B. Quennehen, A. Scharwzenboeck, J. F. Gayet, and
918 K. S. Law, “Airborne measurements of aerosol optical properties related to early spring transport of
919 mid-latitude sources into the Arctic », *Atm. Chem. Phys.* **9**, 27791–27836, (2009).
- 920
- 921 [16] V.F. Freudenthaler et al., “Depolarization ratio profiling at several wavelengths in pure Saharan
922 dust during SAMUM 2006”, *Tellus*, **61B**, 165–179, (2009).
- 923
- 924 [17] MI Mishchenko, L.D. Travis and A.A. Lacis, “Scattering, absorption and emission of Light by
925 small particles”, 3rd edition, Cambridge University Press, UK, (2002).
- 926
- 927 [18] M. Kahnert, T. Nousiainen and B. Veihelmann,” Spherical and spheroidal model particles as an
928 error source in aerosol climate forcing and radiance computations: a case study for feldspar aerosols.
929 *J Geophys Res*, 110:D18S13, (2005).

930 [19] T. Nousiainen et al., "Optical modeling of mineral dust particles: a review", *J. Quant. Spec.*
931 *Rad. Tranf.*, **110**, 1261-1279, (2009).

932

933 [20] N. Kolev et al., "Investigation of the aerosol structure over an urban area using a polarization
934 Lidar", *J. Environ. Monit.*, **19**, 834-840, (2004).

935

936 [21] A. Miffre, G. David, B. Thomas, P. Rairoux, A.M. Fjaeraa, N.I. Kristiansen, A. Stohl, Volcanic
937 aerosol optical properties and phase partitioning behavior after long-range advection characterized by
938 UV-Lidar measurements, *Atm. Env.*, accepted for publication, doi:10.1016/j.atmosenv.2011.03.057,
939 (2011).

940

941 [22] A. Miffre, G. David, B. Thomas, M. Abou Chacra and P. Rairoux, "Interpretation of accurate
942 UV-Polarization Lidar measurements: Application to volcanic ash number concentration retrieval",
943 *J. Atm. Ocean. Tech.*, accepted for publication, (2011).

944

945 [23] A. Miffre, G. David, B. Thomas, P. Rairoux, "Characterization of Iceland volcanic aerosols by
946 UV-polarization Lidar at Lyon, SW Europe", *Proceedings of SPIE*, **7832**, DOI: 10.1117/12.869019,
947 (2010).

948

949 [24] A. Miffre, G. David, B. Thomas, and P. Rairoux, "Atmospheric non-spherical particles optical
950 properties from UV-polarization lidar and scattering matrix", *Geophys. Res. Lett.*, **38**, L16804,
951 (2011).

952 [25] A. Miffre et al., "Aerosol load study in urban area by Lidar and numerical model", *Atm. Env.*,
953 **44**, 1152-1161, (2010).

954

955 [26] H. Adachi, T. Shibata, Y. Iwasaka and M. Fujiwara, "Calibration method for the lidar-observed
956 stratospheric depolarization ratio in the presence of liquid aerosol particles", *Appl. Opt.*, **40**, 6587-
957 6595, (2001).

958

959 [27] R.M. Measures, "Laser Remote Sensing, Fundamentals and applications", Krieger Ed. (1992).

960

961 [28] R.B Miles, W.R. Lempert and J.N. Forkey, "Laser Rayleigh scattering : a review", *Meas. Sci.*
962 *Technol.* **12**, R33–R51, (2000).

963

964 [29] A. Behrendt and T. Nakamura, "Calculation of the calibration constant of polarization lidar
965 and its dependency on atmospheric temperature", *Opt. Exp.*, **10**, 805-817, (2002).

966

967 [30] D.M. Winker and M.T. Osborn, "Preliminary analysis of observations of the Pinatubo volcanic
968 cloud with a polarization-sensitive lidar", *Geophys. Res. Lett.*, **19**, 171-174, (1992).

969

970 [31] J.D. Klett, "Lidar inversion with variable backscatter/extinction ratios", *Appl. Opt.*, **24**, 1638-
971 1643, (1985).

972

- 973 [32] T.L. Anderson, S.J. Masonis, D.S. Covert, R.J. Charlson, M.J. Rood, “In situ measurement of
974 the aerosol extinction-to-backscatter ratio at a polluted continental site”, *J. Geophys. Res.* **105**,
975 26907-26915, (2000).
- 976
- 977 [33] T. Murayama et al., “Application of lidar depolarization measurement in the atmospheric
978 boundary layer: Effects of dust and sea-salt particles”, *J. Geophys. Res.*, **104**, 31781-31792, (1999).
- 979
- 980
- 981 [34] J. Biele, G. Beyerle and G. Baumgarten, “Polarization lidar: corrections of instrumental effects »
982 *Opt. Exp.*, **7**, 427-435, (2000).
- 983
- 984 [35] J. Reichardt, R. Baumgart and T.J. McGee, “Three-signal method for accurate measurements
985 of depolarization ratio with lidar », *Appl. Opt.*, **42**, 4909-4913, (2003).
- 986
- 987 [36] J.M. Alvarez, M.A. Vaughan, C.A. Hostetler, W.H. Hunt and D.M. Winker, “Calibration
988 technique for polarization-sensitive Lidars”, *J. Atm. Ocean. Tech.*, **23**, 683-699, (2006).
- 989
- 990 [37] I. Mattis et al., ‘Systematic error of lidar profiles caused by a polarization-dependent receiver
991 transmission: quantification and error correction scheme », *Appl. Opt.*, **48**, 2742-2751, (2009).
- 992
- 993 [38] A. Bucholtz, “Rayleigh-scattering calculations for the terrestrial atmosphere”, *Appl. Opt.* **34**,
994 2765-2773, (1995).
- 995
- 996 [39] A. Miffre, M. Jacquy, M. Büchner, G. Tréneç, and J. Vigué, « Lithium atom interferometer
997 using laser diffraction: description and experiments », *Eur. Phys. J. D*, **33**, 99–112 (2005).

998

999 [40] G. Roy and N. Roy, “Relation between circular and linear depolarization ratios under multiple-
1000 scattering conditions”, *Appl. Opt.* **47**, 6563-6569, (2007).

1001

1002 [41] B. Tatarov and I. Kolev, ‘Experimental determination of the multiple-scattering effect on the
1003 lidar-signal polarization characteristics during liquid and solid-phase precipitation », *Appl. Phys. B*
1004 **73**, 261–268 (2001).

1005

1006 [42] B. Tatarov, T. Trifonov, B. Kaprielov, I. Kolev, “Dependence of the lidar signal depolarization
1007 on the receiver’s field of view in the sounding of fog and clouds”, *Appl. Phys. B* **71**, 593–600 (2000).

1008

1009 [43] J.H. Seinfeld and S.N. Pandis, “Atmospheric chemistry and physics: from air pollution to
1010 climate change”, John Wiley & Sons, (2006).

1011

1012 [44] T. Sakai et al., “Backscattering linear depolarization ratio measurements of mineral, sea-salt,
1013 and ammonium sulfate particles simulated in a laboratory chamber”, *Appl. Opt.* **49**, 4441-4449,
1014 (2010).

1015

1016 [45] M. Esselborn et al., “Airborne high spectral resolution lidar for measuring aerosol extinction and
1017 backscatter coefficients”, *Appl. Opt.* **47**, 346-358, (2008).

1018

1019 [46] M. Ndour P. Conchon, B. D'Anna Barbara; O. Ka and C. George, “Photochemistry of mineral
1020 dust surface as a potential atmospheric renoxification process”, *Geophys. Res. Lett.*, **36**,
1021 2008GL036662, (2009).

1022

1023 [47] D. D. Duncan and M.E. Thomas, “Particle shape as revealed by spectral depolarization”, *Appl.*
1024 *Opt.* **46**, 6185-6191, (2007).

1025

1026 [48] T. Somekwa et al., “A new concept to characterize nonspherical particles from multi-
1027 wavelength depolarization ratios based on T-matrix computation”, *Part. Part. Syst. Charact.*, **25**, 49-
1028 53, (2008).

1029

1030 **List of figures and table captions**

1031 **Fig.1** System bias affecting the dual-wavelength polarization Lidar measurement: (a) presence of a
1032 small unpolarized component in the emitted laser beam, (b): imperfect separation of polarization
1033 components, (c): misalignment between the transmitter and receiver polarization axes, (d): role of the
1034 dichroic beamsplitter introduced for dual-wavelength detection. Top schemes represent the studied
1035 system bias while bottom graphs present the relative error on δ for different values of the bias
1036 parameter (ϵ , $CT_{//}$ and CT_{\perp} , φ and θ_0).

1037

1038 **Fig.2** Sky background contribution to the Lidar intensity. (a) Sun scattering plane geometry and
1039 orientation with respect to the Lidar laser source and the detector polarization $\{//,\perp\}$ -axes. The
1040 emission laser is oriented to the East, and the angle between the solar scattering plane and the East is
1041 $\pi/2 - h$. (b) Measured sky background intensity I_{sb} on each polarization $\{//,\perp\}$ -axis as a function of
1042 the solar local angle on July 3rd 2011 at Lyon.

1043

1044 **Fig.3** Top view of the Lidar station with the laser head, the emitting optics (detailed in the dashed
1045 below box), the receiving optics (elliptical mirror (M_E), telescope) and the Lidar detector D. The
1046 laser beam is emitted vertically, along the z-altitude axis.

1047

1048 **Fig.4** (a) Top view of our home-built UV-VIS polarization Lidar detector D. (b) 3D-exploded side
1049 view of each polarization channel (UV, VIS) composed of two PBC's , one IF_λ and a PMT.

1050

1051 **Fig.5** Laboratory test-bench with numerical aperture $f/3$ to simulate backscattered photons from the
1052 atmosphere. The top scheme is used for measuring the DB_λ reflectivity while the bottom scheme
1053 enables the T_p , R_s -measurements of the PBC's polarization properties, using the $\lambda/2$ plate to control
1054 the incident polarization.

1055

1056 **Fig.6** Calibration curves obtained in the UV and the VIS with corresponding residue plot.

1057

1058 **Fig.7** Time-altitude maps of the parallel and perpendicular particle backscattering coefficient $\beta_{p,//}$ and
1059 $\beta_{p,\perp}$ and the corresponding particle depolarization ratio δ_p , in the UV and the visible spectral range on
1060 October 18th 2011 at Lyon between 13h30 and 18h. The color scales have been adjusted on each map
1061 to enhance the achieved sensitivity in the UV and in the VIS. In between each 4000 laser shots-
1062 vertical profile, the laser has been shut down during 4 minutes.

1063

1064 **Fig.8** Vertical profiles of $\beta_{p,//}$, $\beta_{p,\perp}$ and δ_p on October 18th 2011 at 14h45 at Lyon in the UV (blue)
1065 and the VIS (green). Error bars on $\beta_{p,//}$ are calculated by using the maximum and minimum values of
1066 S_p in the Klett's algorithm. Error bars on $\beta_{p,\perp}$ are derived from the section 2-derived relation : $\beta_{p,\perp} =$
1067 $(R_{//}\delta - \delta_m) \times \beta_{m,//}$ while error bars on δ_p are calculated by applying equation (5).

1068

1069 **Tab. 1** Optical specifications of the emission laser, the emitter optics and the Lidar receiver.

1070

1071 **Tab. 2** Optical specifications of the UV-VIS polarization detector D.

1072

1073

1074

1075

1076

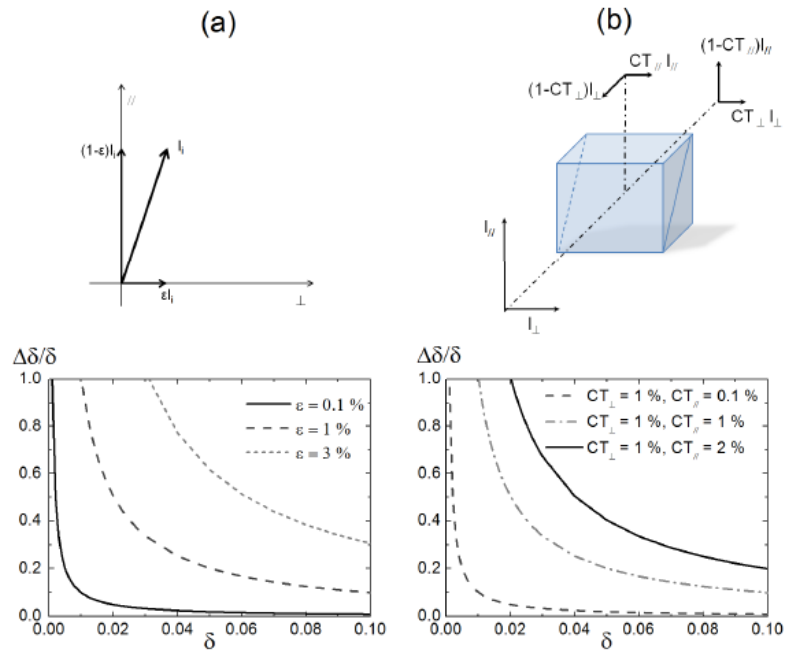
1077

1078

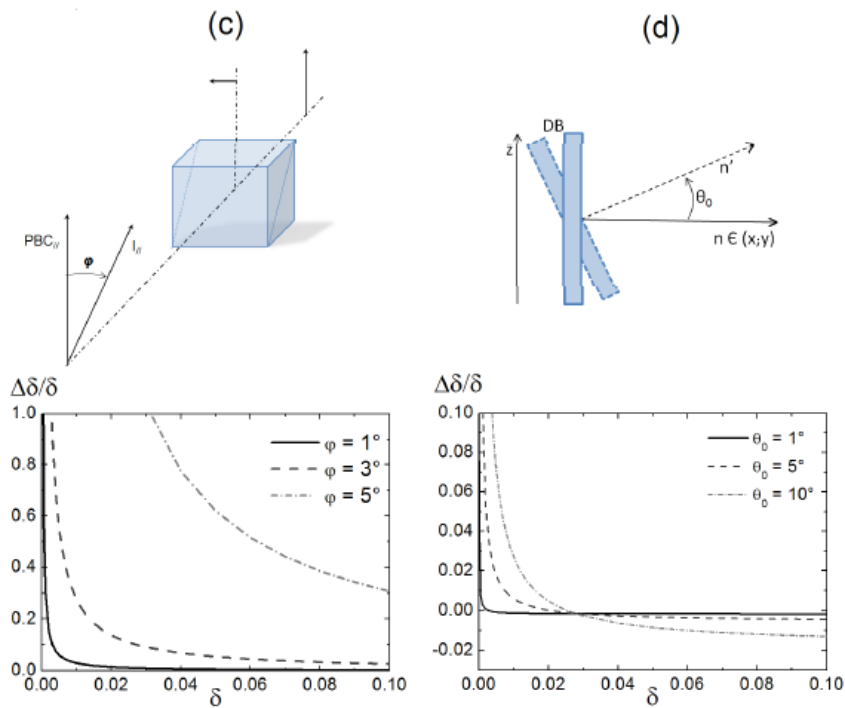
1079

1080

1081

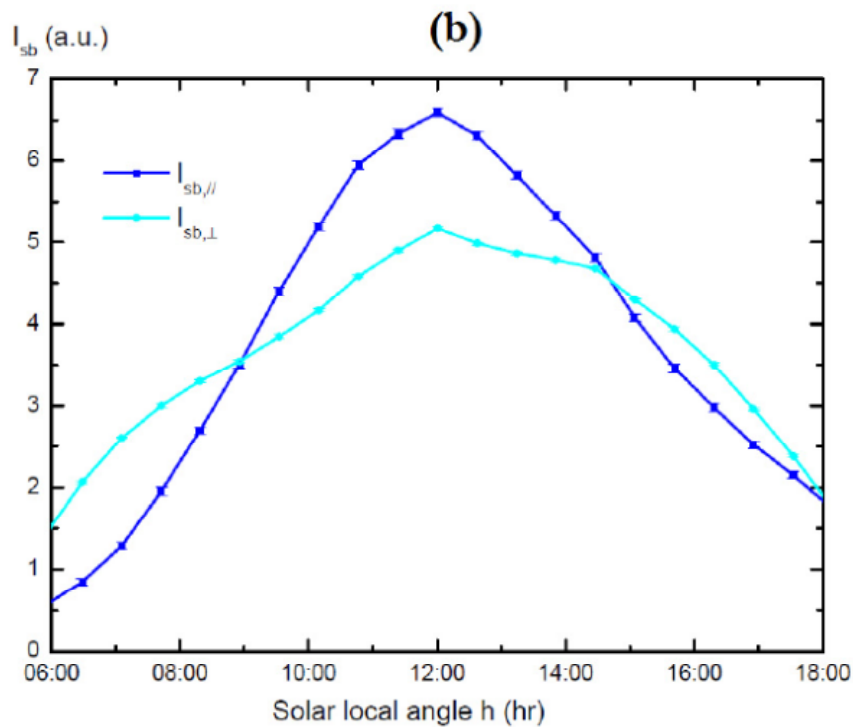
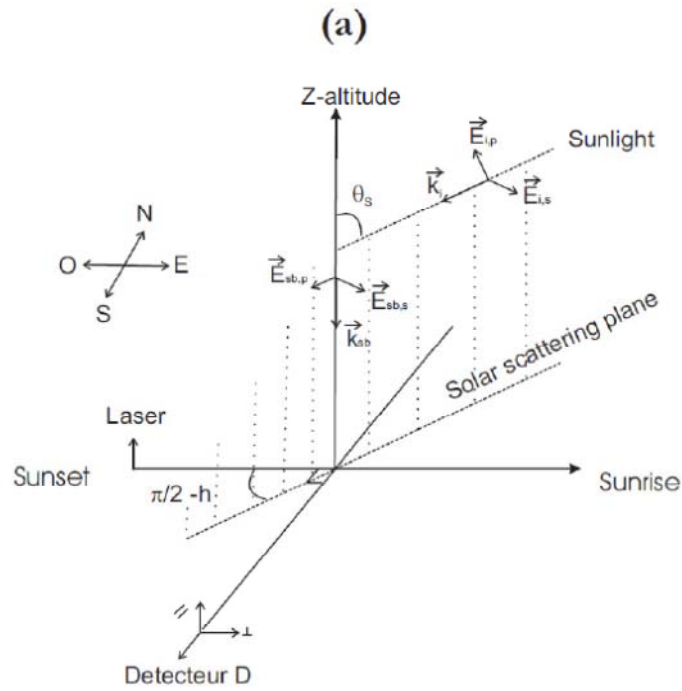


1082



1088

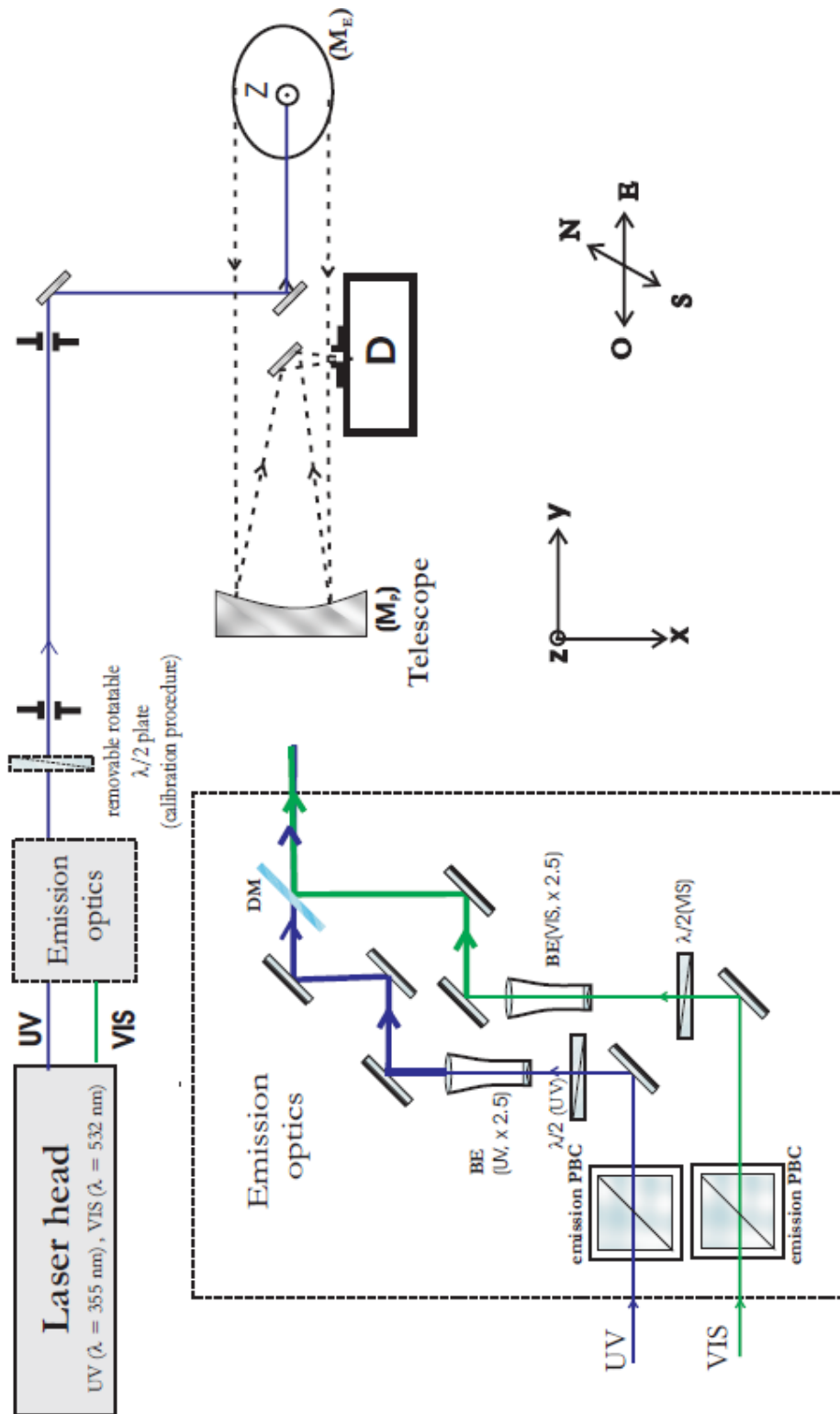
1083 **Fig.1** System bias affecting the dual-wavelength polarization Lidar measurement: (a) presence of a
 1084 small unpolarized component in the emitted laser beam, (b): imperfect separation of polarization
 1085 components, (c): misalignment between the transmitter and receiver polarization axes, (d): role of the
 1086 dichroic beamsplitter introduced for dual-wavelength detection. Top schemes represent the studied
 1087 system bias while bottom graphs present the relative error on δ for different values of the bias
 1088 parameter (ϵ , CT_{\parallel} and CT_{\perp} , φ and θ_0).



1089

1090

1091 **Fig.2** Sky background contribution to the Lidar intensity. (a) Sun scattering plane geometry and
 1092 orientation with respect to the Lidar laser source and the detector polarization $\{//,\perp\}$ -axes. The
 1093 emission laser is oriented to the East, and the angle between the solar scattering plane and the East is
 1094 $\pi/2 - h$. (b) Measured sky background intensity I_{sb} on each polarization $\{//,\perp\}$ -axis as a function of
 1095 the solar local angle on July 3rd 2011 at Lyon.



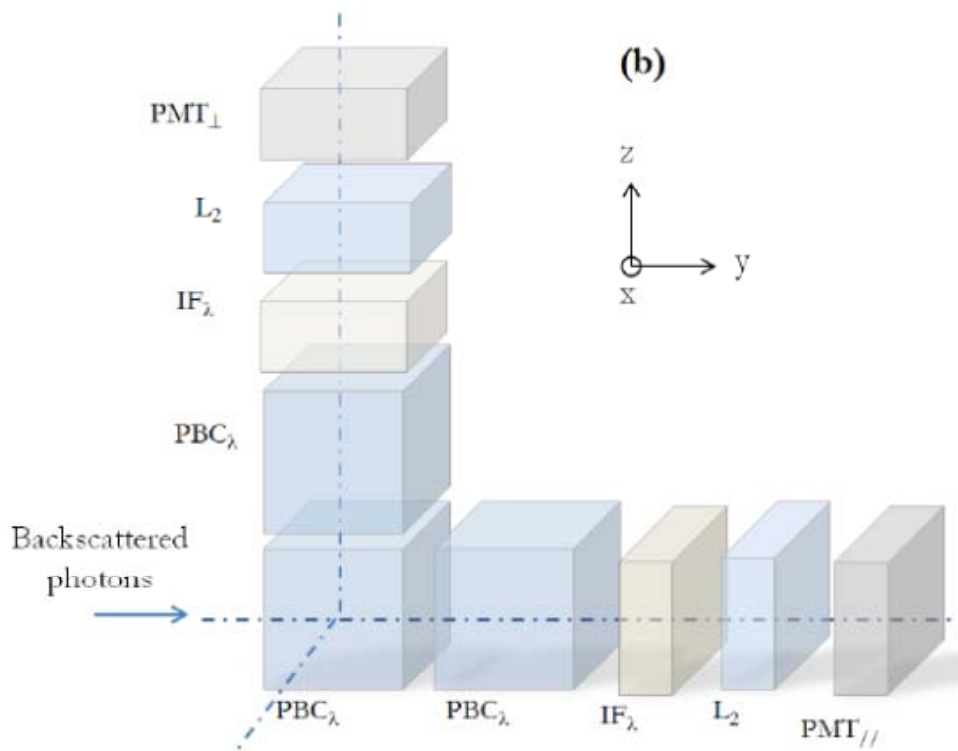
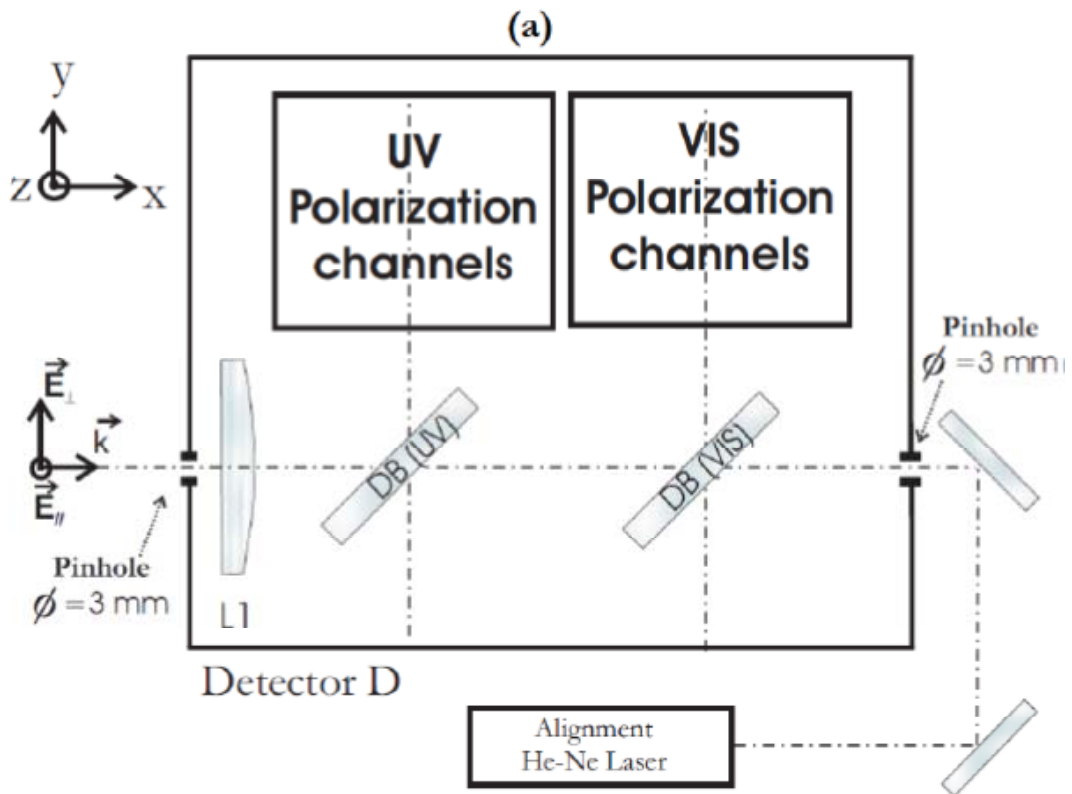
1096

1097

1098 **Fig.3** Top view of the Lidar station with the laser head, the emitting optics (detailed in the dashed

1099 below box), the receiving optics (elliptical mirror (M_E), telescope) and the Lidar detector D. The

1100 laser beam is emitted vertically, along the z-altitude axis.



1101

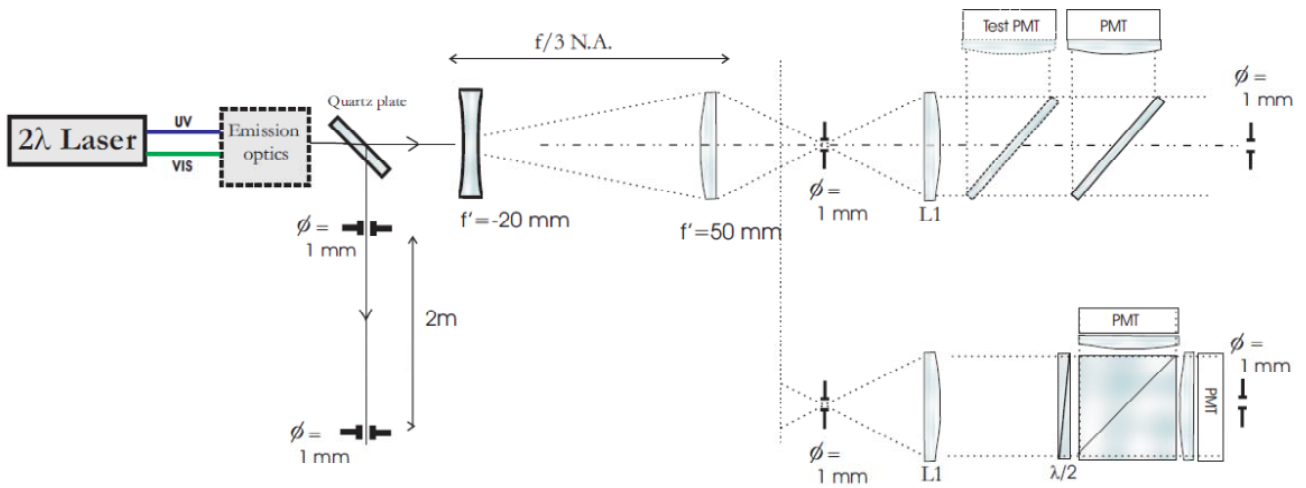
1102

1103

1104 **Fig.4** (a) Top view of our home-built UV-VIS polarization Lidar detector D. (b) 3D-exploded side

1105 view of each polarization channel (UV, VIS) composed of two PBC's , one IF_λ and a PMT.

1106



1107

1108

1109 **Fig.5** Laboratory test-bench with numerical aperture $f/3$ to simulate backscattered photons from the
1110 atmosphere. The top scheme is used for measuring the DB_λ reflectivity while the bottom scheme
1111 enables the T_p , R_s -measurements of the PBC's polarization properties, using the $\lambda/2$ plate to control
1112 the incident polarization.

1113

1114

1115

1116

1117

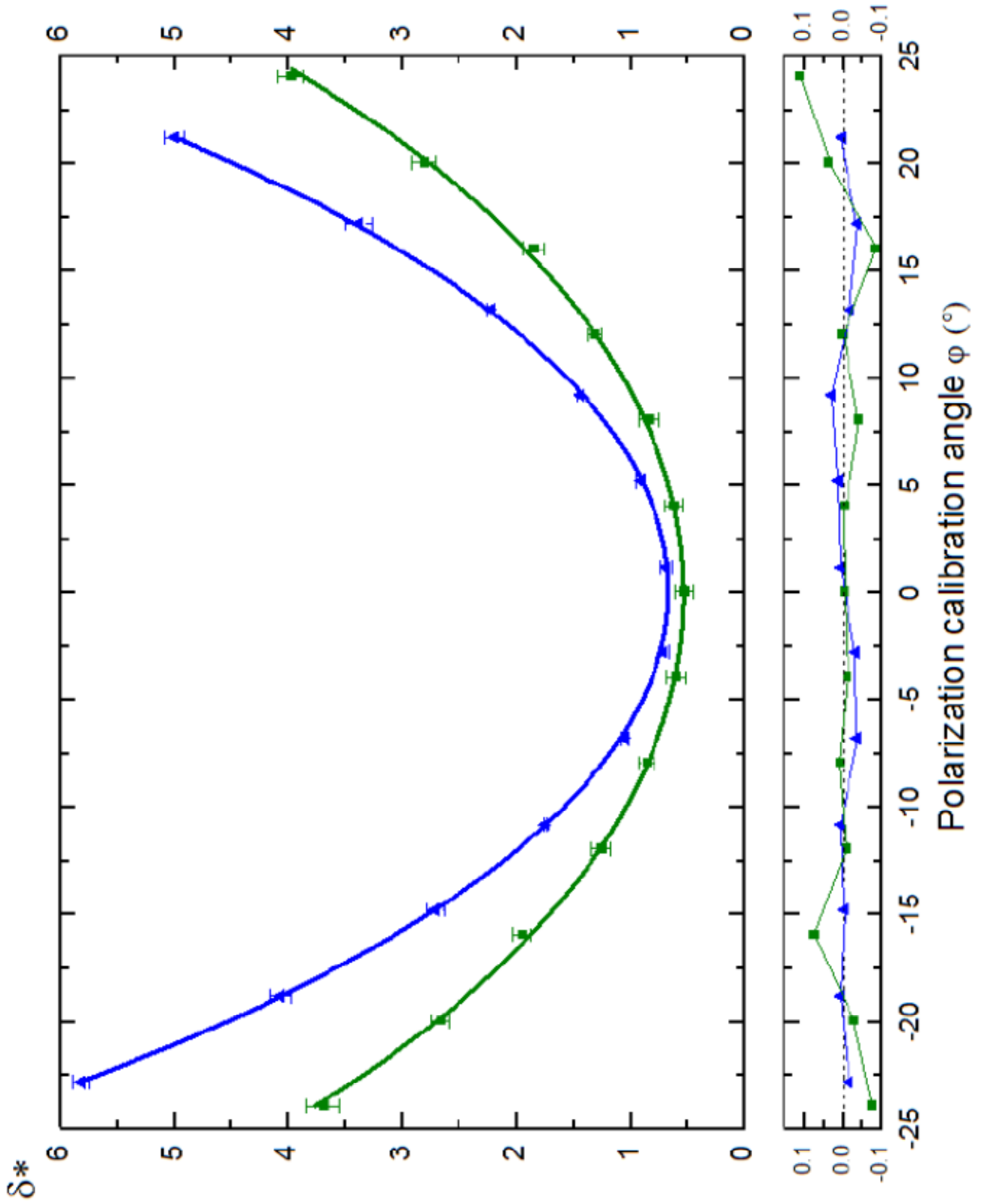
1118

1119

1120

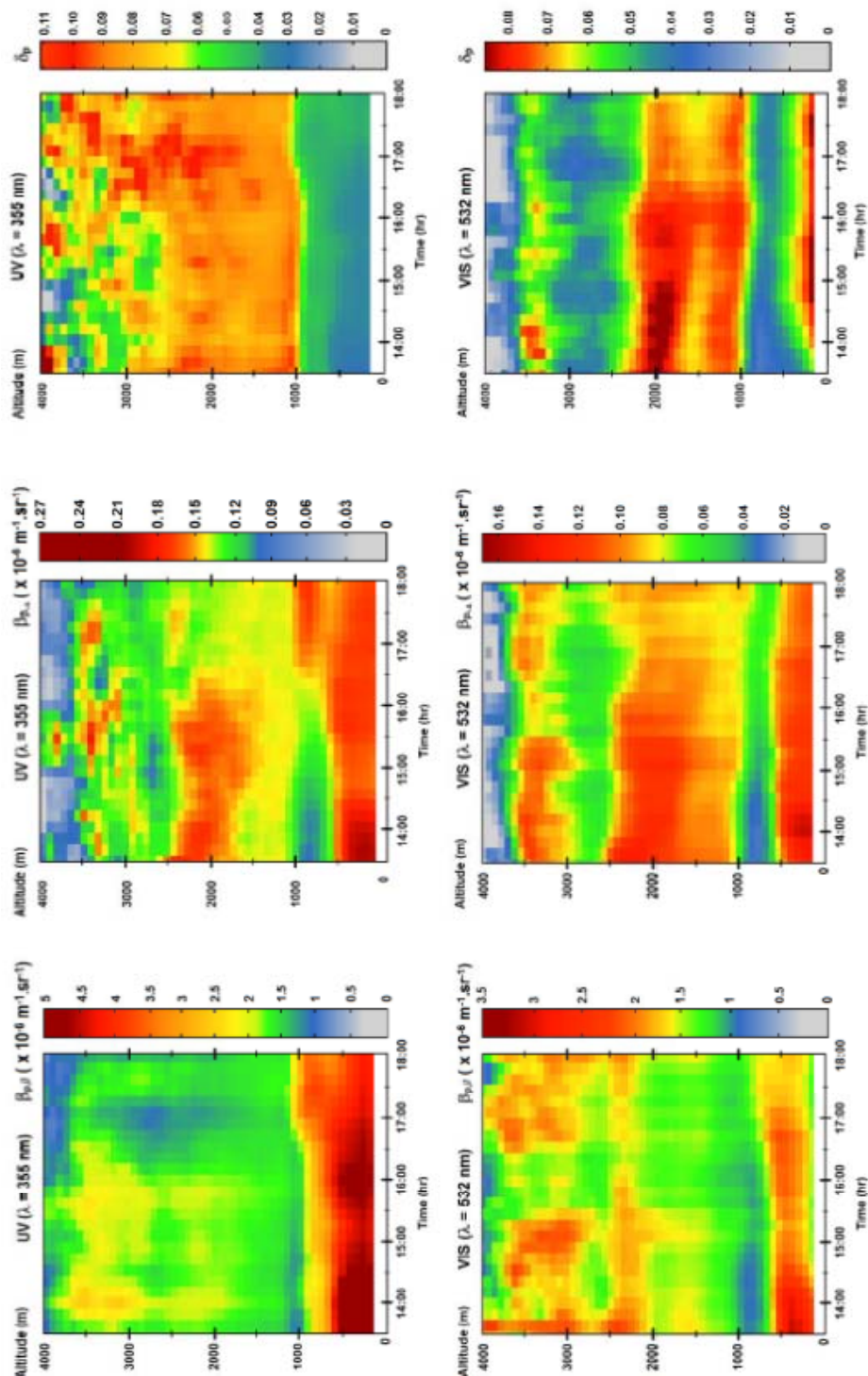
1121

1122



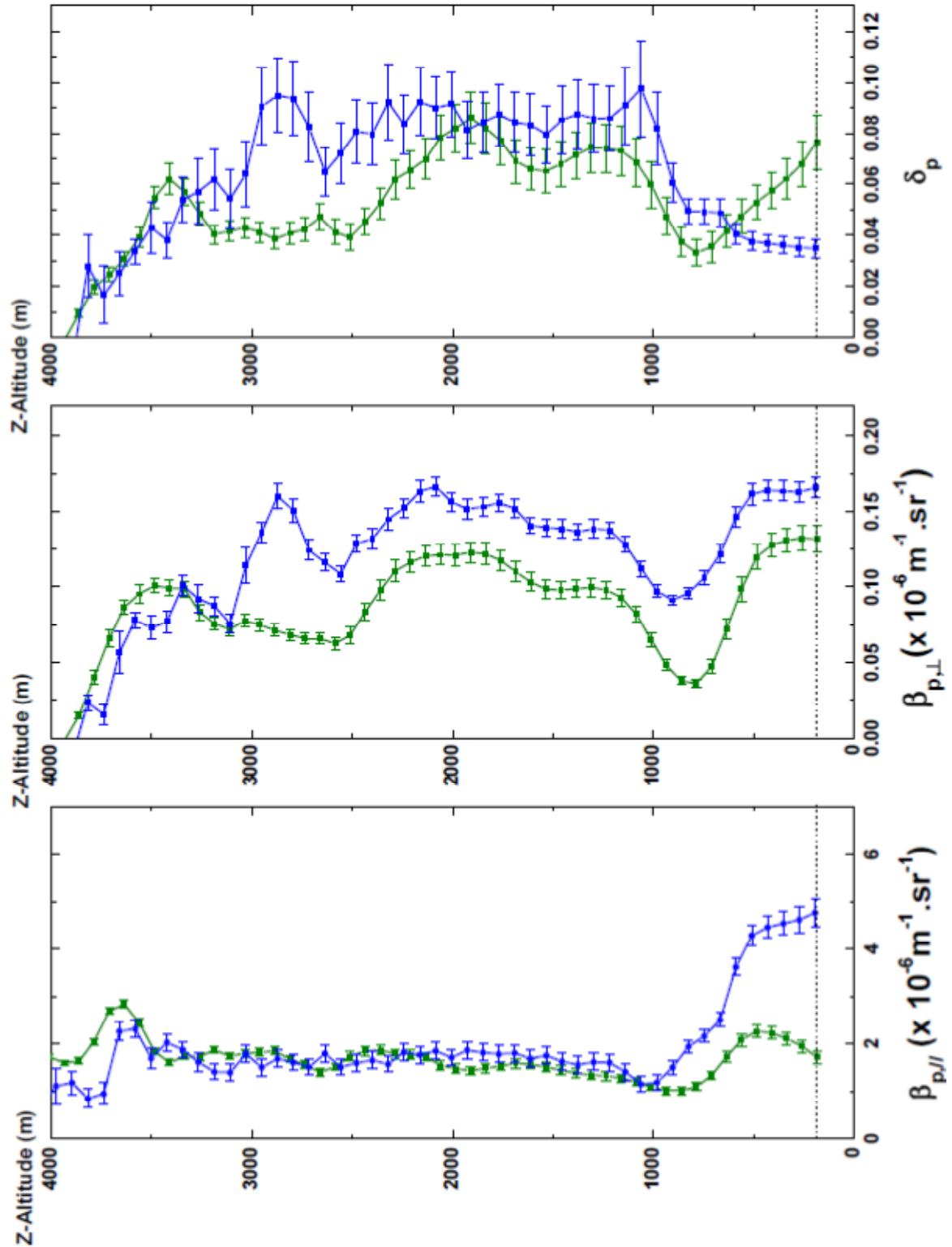
1123

1124 **Fig.6** Calibration curves obtained in the UV and the VIS with corresponding residue plot.



1125

1126 **Fig.7** Time-altitude maps of the parallel and perpendicular particle backscattering coefficient $\beta_{p,\parallel}$ and
 1127 $\beta_{p,\perp}$ and the corresponding particle depolarization ratio δ_p , in the UV and the visible spectral range on
 1128 October 18th 2011 at Lyon between 13h30 and 18h. The color scales have been adjusted on each map
 1129 to enhance the achieved sensitivity in the UV and in the VIS. In between each 4000 laser shots-
 1130 vertical profile, the laser has been shut down during 4 minutes.



1131

1132 **Fig.8** Vertical profiles of $\beta_{p,\parallel}$, $\beta_{p,\perp}$ and δ_p on October 18th 2011 at 14h45 at Lyon in the UV (blue)

1133 and the VIS (green). Error bars on $\beta_{p,\parallel}$ are calculated by using the maximum and minimum values of

1134 S_p in the Klett's algorithm. Error bars on $\beta_{p,\perp}$ are derived from the section 2-derived relation : $\beta_{p,\perp} =$

1135 $(R_{\parallel}\delta - \delta_m) \times \beta_{m,\parallel}$ while error bars on δ_p are calculated by applying equation (5).

UV-VIS Lidar laser source		
Pulse energy	10 mJ (UV), 20 mJ (VIS)	
Pulse duration	10 ns	
Pulse repetition rate	10 Hz	
Laser beam initial divergence	1 mrad	
Laser initial polarization rate (I_p/I_s)	> 100:1	
Emitter optics		
Emission PBC (UPBS- λ -100)	$T_p/T_s > 250$	$T_p/T_s > 500$
Beam expanders (Bmx λ 2,5x)	$\times 2.5$	$\times 2.5$
Dichroic mirror (SWP-45-R _s 532-T _s 355-PW)	$T_s > 0.995$	$R_s > 0.995$
Emission mirror (NB1-K)	$R_s > 0.995$	$R_p > 0.99$
Lidar receiver		
Primary mirror focal length	600 mm	
Primary mirror diameter	200 mm	
Secondary mirror diameter	50 mm	
Pinhole diameter	3 mm	
Field of view	2.5 mrad	

1137

1138 **Tab.1** Optical specifications of the emission laser, the emitter optics and the Lidar receiver.

1139

1140

1141

1142

1143

1144

1145

UV-VIS polarization detector D		
Dichroic beamsplitter (355 nm)	$R_p = (72.3 \pm 0.5) \%$	$R_s = (94.3 \pm 0.5) \%$
Dichroic beamsplitters (532 nm)	$R_p = (99.9 \pm 0.5) \%$	$R_s = (86.7 \pm 0.5) \%$
PBC ₁ (UPBS-UV-100)	$R_{s,1} = 1.000$	$T_{p,1} = 0.998$
PBC ₂ (UPBS-UV-100)	$R_{s,2} = 0.980$	$T_{p,2} = 0.992$
PBC ₃ (UPBS-UV-100)	$R_{s,3} = 0.998$	$T_{p,3} = 0.996$
IF _λ center wavelength	354.94 nm (UV)	532.14 nm (VIS)
IF _λ filter bandwidth	0.35 nm (UV)	0.52 nm (VIS)

1146

1147 **Tab.2** Optical specifications of the UV-VIS polarization detector D.